Dinantian geothermal potential

S. Nelskamp, J.P.T. Foeken, J.G. Veldkamp
(TNO)

April 30, 2022

Summary

In order to calculate the geothermal potential maps of the Carboniferous Dinantian in the wider Dutch, North-Rhine Westphalia, Belgium and French region, temperature, permeability and heat in place maps have been constructed and calculated. Maps are generated from information made available by the DGE Rollout consortium, and literature data. It builds on Dinantian depth and thickness maps that were constructed as parts of previous DGE Rollout deliverables.

A temperature map for the Top Dinantian was constructed by integrating temperature data derived from regional 2D maps, 3D temperature models and well data. Because of the different data formats a workflow was adopted to (re)calculate available temperature data into (local) temperature gradients (°C/km), merge the gradients into a single map and then use the resulting cross-border temperature gradient map together with the Top Dinantian map to calculate the temperature at the Top Dinantian. In this way, the structural grain (presence and incorporation of (local) faults) is preserved, challenges related to sparse temperature data coverage are alleviated and effects resulting from differences in burial, compaction and lithology are negated.

Regional permeability maps have been constructed for the Dinantian. Based on existing literature reviews, it is assumed that Dinantian permeability is largely governed by structural (fault permeability) and diagenetic (karstification) processes. Using literature data on fault damage zone width, fracture permeability, fault displacement and length, combined with carbonate rock properties (permeability measurements on Dinantian core plugs) and karst permeability assumptions), minimum, average and maximum permeability maps have been calculated.

A Heat in Place (HIP) map was calculated for the Dinantian for areas where the Dinantian thickness is known. The HIP varies from 50 – 200 GJ/m² in the North-Rhine Westphalia and Wallonia regions to up to 400 GJ/m² in the Flanders region. For the most part, Dinantian thickness is unknown in the Netherlands, hence the HIP here is sparse.

Using the ThermoGIS method with flow property (the permeability maps), maps of the geothermal power that can be extracted by a heat exchanger were calculated. Depending on the permeability scenarios, minimum, average and maximum potential power maps have been compiled.

Limitations of the various compiled maps include:

- Uncertainty in the temperature map is largely caused by sparse temperature data (or models) in certain regions. With the addition of new temperature data, the map will improve in accuracy.
- Sparse permeability measurements on Dinantian rock plugs, as well as incomplete understanding of the spatial continuity of permeability in fault zones, requires that permeability concepts and/or assumptions need to be adopted in order to correlate permeability to structural concepts (fault displacement, fault damage zone) as well as sedimentological concepts (karstification). Calibrating the maps with new permeability measurements on rock plugs will improve the map.
- Only few of the faults used for the permeability assessment have been actually mapped in the Dinantian but rather extrapolated from the Base Permian/Top Carboniferous. Therefore additional uncertainty is related to the actual presence and precise location of these faults and associated assumed high permeability zones.

- The generated heat in place maps do not include flow property information. Therefore they do not provide information on the actual geothermal potential on a local scale. The HIP maps do provide regional information, and as such should only be used to for a first order, regional assessment of the heat potential.

Contents

1 Introduction

Having a hot subsurface does not necessarily mean that heat can be extracted and used for heating or electricity production, or, in other words, it does not always imply the presence of geothermal potential referring to conventional geothermal systems that rely on matrix and/or fracture permeability, which may be enhanced by applying stimulation techniques such as fracking.

Shown on the basis of the heat pyramid in Figure 1 is the *heat in place* (HIP), which is defined as the maximum theoretically extractable heat energy in an aquifer, relative to an (arbitrary) reference temperature (Muffler & Cataldi (1978)). Following Kramers et al. (2012), the *potential recoverable heat* (PRH) is the heat which can be extracted from the aquifer, unconstrained by economic limitations and irrespective of flow properties (Van Wees et al. (2012)). The *recoverable heat* (RH) is the extractable heat when the two limiting factors transmissivity and economy are considered. Finally, the matched recoverable heat (MRH) is the part of the RH that is met by actual demand. From the bottom to the top of the pyramid, the calculation of the geothermal potential becomes increasingly data demanding. This data is generally lacking, and subsequently estimates are subject to large uncertainty.

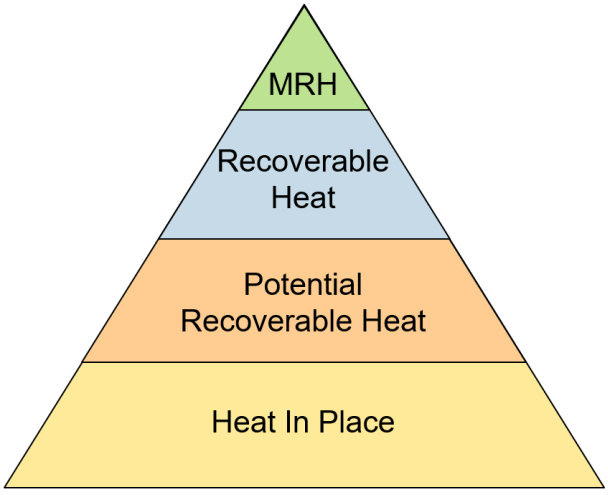

Figure 1 Filtering pyramid showing the total heat content for HIP (Heat in Place), PRH (Potential Recoverable Heat) and RH (Recoverable Heat). After Kramers et al. (2012).

Geothermal potential can be defined in different ways, such as technical or economic potential (Van Wees et al. (2012)). Consequently, the unit of potential can be joule (energy), power (energy / time), achievable flow rate or cost (such as unit technical cost, or cost per unit energy produced). Economic potential, being dependent on costs and revenues that may rapidly change in time, is volatile. The technical potential is also subject to change depending on technological developments, but generally less than economic potential.

In order to calculate HIP, PRH and RH regional information on the relevant aquifer properties (notably depth, thickness, porosity and permeability) and temperature is required. For calculating the economic potential, an economic model is required which takes financial aspects into account.

This report describes how temperature (chapter 2) and permeability maps (chapter 3) were generated from information made available by the DGE Rollout consortium and literature data. It builds on Dinantian depth and thickness maps that were constructed as previous DGE Rollout deliverables. Further, the ThermoGIS software (Kramers et al. (2012); Van Wees et al. (2012);

Vrijlandt et al. (2020)) was used to combine the constructed maps and calculate indicative geothermal potential maps (chapter 4). Chapter 5 draws conclusions from the resulting potential maps and recommends future improvements.

2 Temperature

A temperature map for the Top Dinantian was constructed by integrating regional temperature data from France, Belgium (Wallonia, Flanders), North Rhine-Westphalia and The Netherlands (3D models, well data).

A summary of the adopted workflow to construct the temperature map is:

1. Compile available temperature data (3D models, well data).
2. Use the harmonized Top Dinantian depth map to calculate a temperature gradient map for each region. Temperature gradients are calculated from 3D temperature models, 2D temperature maps or from borehole temperature data from well data (1D).
3. Use convergent gridder in Petrel to construct a new regional temperature gradient map covering the lateral extend of the Top Dinantian.
4. Calculate the temperature at the Top Dinantian from the aquifer depth and temperature gradient maps (assuming 10°C surface temp).

2.1 Workflow

Information on temperatures in Dinantian units are available from 3D temperature models to 1D well data with borehole temperature (BHT) measurements. Because of the different formats it was decided to (re)calculate all available temperature data into (local) temperature gradients (°C/km), merge the gradients into a single map and then use the cross-border gradient map to calculate the temperature at the Top Dinantian. When temperature maps for the Top Dinantian are already present (e.g. the Netherlands, Flanders and NRW) this approach may seem redundant. However, our approach alleviates several important issues related to the temperature map:

- The Top Dinantian depth map has a structural grain, and (local) faults are clearly visible (Figure 2); these would disappear when gridding a new, regional temperature map on point data instead of a gradient map.
- Well data in France and Wallonia are too sparse to grid a detailed temperature map.
- By using a temperature gradient instead of calculating the temperature at the Top Dinantian directly, local/regional effects resulting from differences in burial, compaction and lithology are negated.

For The Netherlands the adopted workflow results in a 3D temperature gradient map; for the well data in Wallonia and France 1D gradients (per well) are calculated. From the available temperature gradients and the harmonized Top Dinantian depth map, a 2D regional temperature map at the Top Dinantian was calculated assuming a regional surface temperature of 10°C:

Temperature_Top Dinantian = Temperature gradient * Depth_Top Dinantian + 10°C

The following workflow was adopted:

1. Compile available temperature data.
   For 1D well data, plot available data versus depth and calculate a temperature gradient for the specific well.
2. For 3D temperature data, check if the model incorporates regional temperature variations or if a single, fixed gradient is used. The latter is checked by intersecting the harmonized depth map with the 3D temperature model. This results in the temperature at Top Dinantian for

the specific region of interest. This temperature map is then divided by the depth map. If originally a single, fixed gradient was used, the newly calculated gradient map results in a smooth gradient map with a peak at a certain °C/km; a regionally calibrated temperature model results in more variation in calculated gradients across the map.

3. Compile all new calculated gradients (from wells and 3D models) and use convergent gridder in Petrel to construct a new regional temperature gradient map for the lateral extend of the Top Dinantian (as mapped in the harmonised Top Dinantian depth map).
4. Calculate the temperature at the Top Dinantian from the depth & gradient map (assuming 10°C surface temp).

2.2 Data: Temperature data and Top Dinantian depth map

Several temperature datasets have been made available:

- Netherlands: 3D temperature model (from the SCAN project (Veldkamp & Hegen (2020);
- Belgium: GeoHeat map (temperature map) for Flanders and well/bore hole temperature data (1D) for Wallonia;
- NRW: 2D temperature map and 3D temperature model (Agemar et al. (2012));
- France: borehole data.

The DGE Rollout harmonised Top Dinantian depth map was used as basis for calculating the Top Dinantian temperature map.

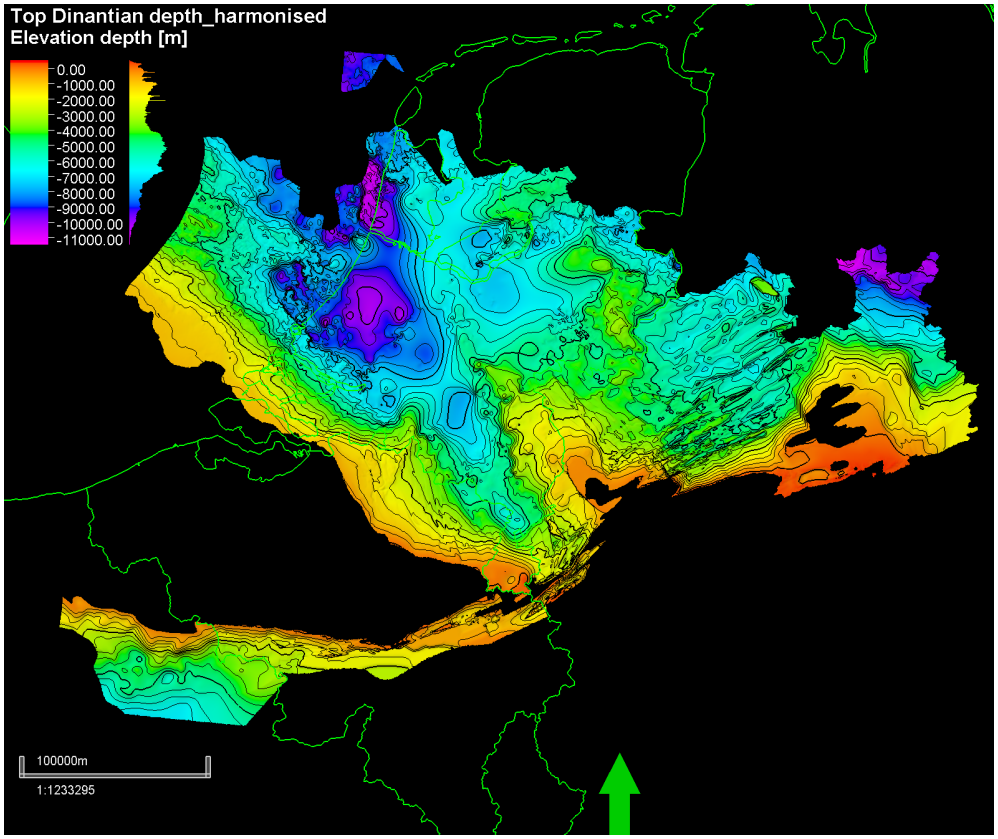

Figure 2 The DGE Rollout harmonised Top Dinantian depth map used to construct the Top Dinantian temperature map.

2.2.1 The Netherlands

For the Netherlands, a national 3D temperature model is available from surface level down to 7000m depth (Figure 3). This 3D model was constructed within the SCAN research project (Veldkamp & Hegen (2020)), and builds on previous work by Békési et al. (2020); Bonté et al. (2012); Gies et al. (2021). The 3D model covers the onshore Netherlands area only. It is based on a 2.5D layer model of the Dutch subsurface constructed from seismic and well data, a set of ~3000 bottom hole temperatures, and temperatures obtained in geothermal wells and observation wells, and handbook rock thermal property values. The data is used in a forward thermal model which uses ES-MDA (Ensemble Kalman – Multiple Data Assimilation) to obtain a good fit between measured and calculated temperatures.

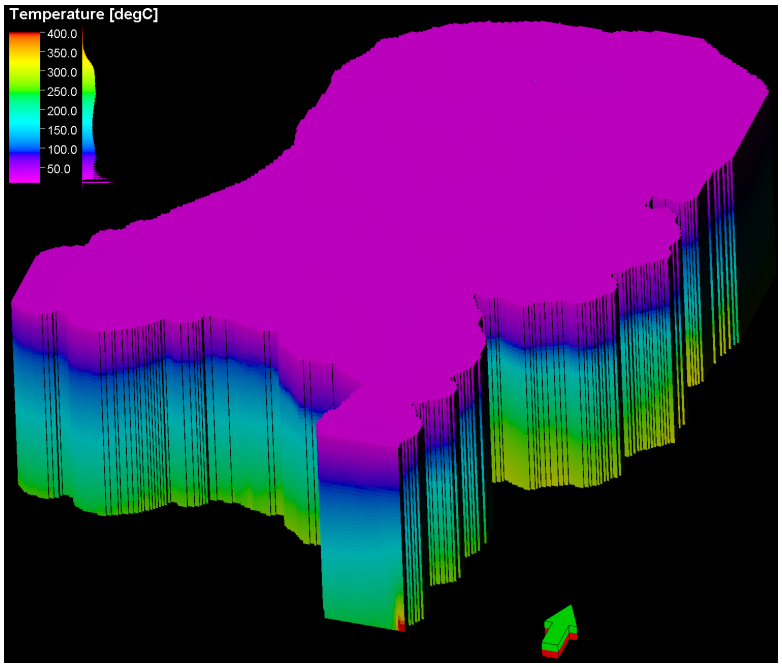

Figure 3: 3D temperature model for The Netherlands, adopted from the SCAN project (Veldkamp and Hegen, 2020).

2.2.2 France

Well data with relevant information (e.g., location depth, penetrated sections, borehole temperature (BHT) measurements) are available for the whole of France (Figure 4). Data were supplied in tables in Excel format. Well temperature data are reported as Borehole Corrected (e.g., Horner correction) and Uncorrected data.

Only one well (Epinoy-1 or EPY-1), reference number 14-3602) is available within the lateral extend of the Dinantian (Figure 4). It penetrated the Namurian section at a depth of -785 m below surface. Corresponding Horner corrected BHT at this depth is 49.2°C.

Based on the same well data, Bonté et al. (2013) constructed a 3D temperature model. Depth horizons (1000 m, 1500 m, 2000 m, 2500 m, 3000 m, 4000 m, 5000 m and 6000 m) were exported from this temperature model and a subset for Northern France were imported in Petrel. Using a simple Kriging routine with high anisotropy, a new 3D temperature model (1000x1000x100m grid cells), was constructed from the Bonté et al. (2013) dataset (Figure 5).

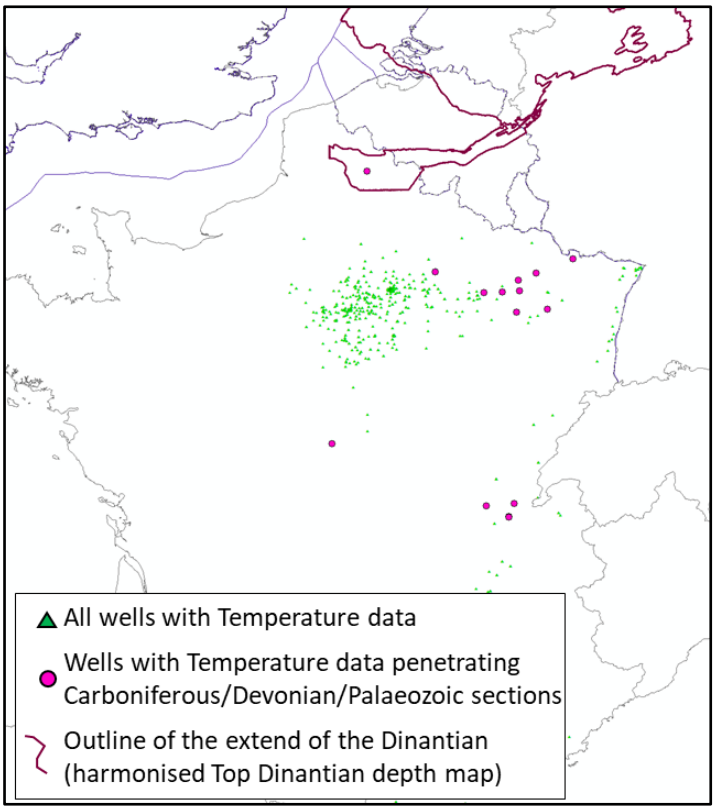

Figure 4 *Locations of well data with borehole temperature measurements in France. Only one well with temperature measurements is available within the extend of the Dinantian (Epinoy-1).*

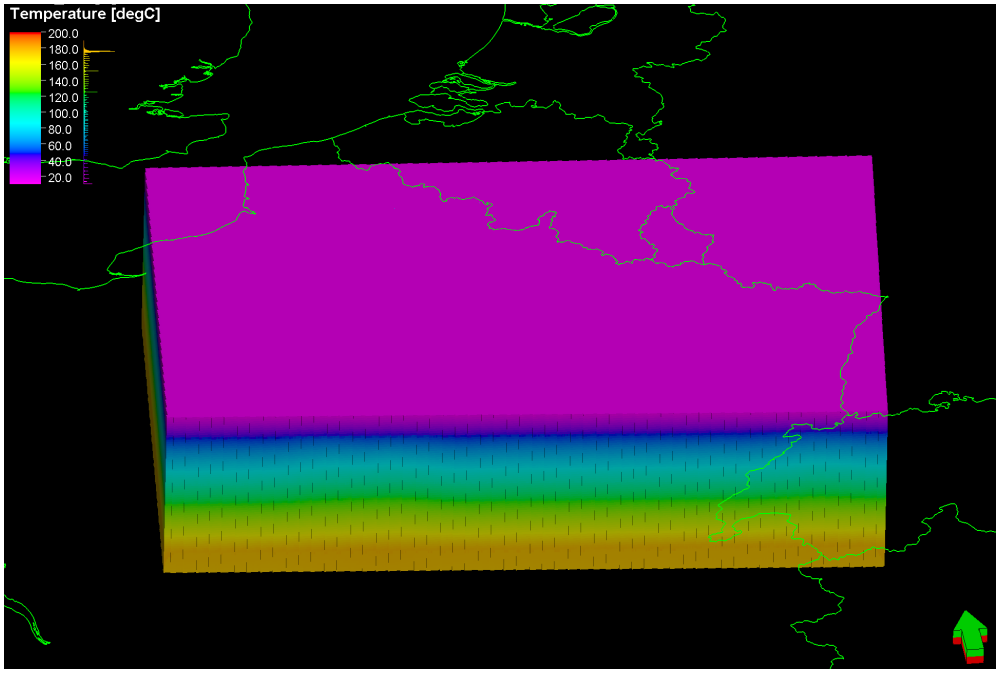

Figure 5 *A simple Kriging routine with high anisotropy was applied to construct a 3D temperature model from the Bonté et al. (2013) temperature data for Northern France.*

2.2.3 North Rhine-Westphalia

Two temperature data sets are available for the North Rhine-Westphalia (NRW) region. The first data set is a 2D grid of the temperature at the Top Dinantian compiled by GD-NRW (Figure 6), hereafter

referred to as the Arndt temperature model. It was made using a constant gradient and the Top Dinantian structural map. The 2D grid (250x250 m grid cells) covers the entire extend of the Dinantian in NRW and ranges from surface temperature to 360°C.

A second temperature data set is derived from a 3D temperature model for the whole of Germany (Agemar et al. (2012)). The model consists of grid cells of 2000x2000x100 meters, grouped in 49 layers. It covers the entire Germany and ranges in depth from 100 to 5000 m below surface (Figure 7A). By intersecting the harmonised Top Dinantian depth map with this 3D temperature model, a temperature map for the Top Dinantian is constructed. Due to the limited depth of the model by Agemar et al. (2012) (max. 5000 m), a significant portion of the Top Dinantian temperature map is missing (Figure 7B).

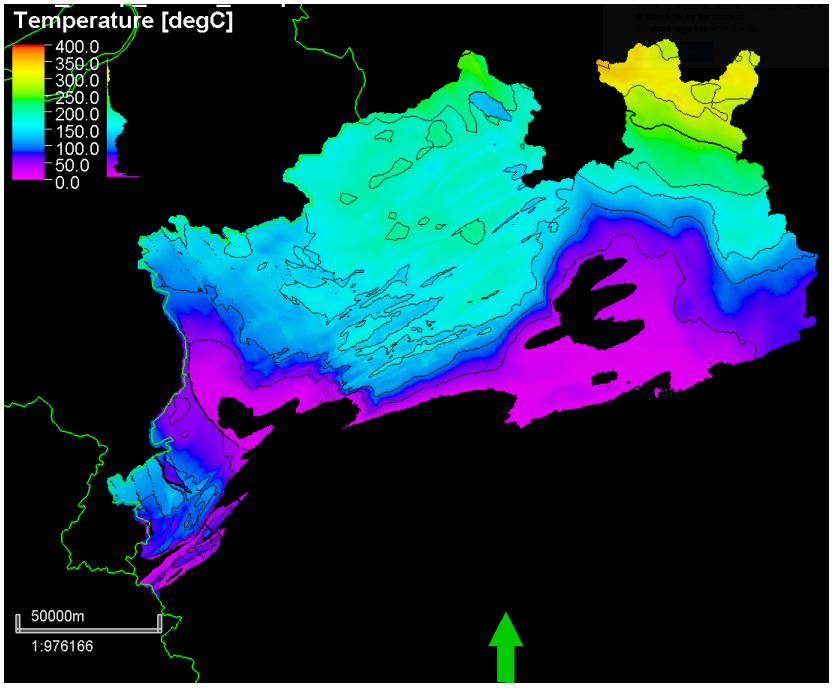

Figure 6 3D temperature model (courtesy M. Arndt, Interreg DGE Rollout). Contour interval 50 °C.

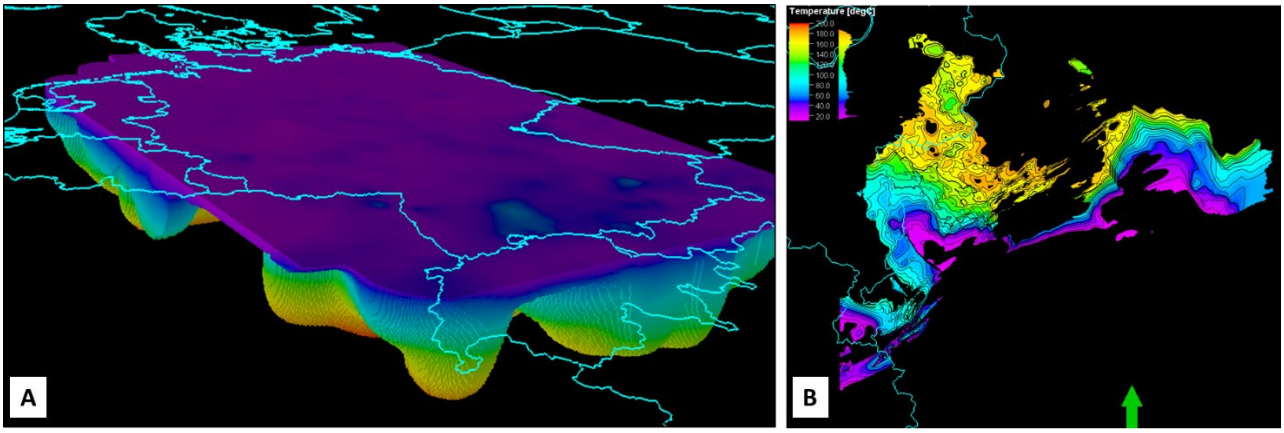

Figure 7 A. Agemar 3D temperature model for Germany (Agemar et al. (2012). B. Map of the temperature at Top Dinantian, resulting from intersecting the harmonized Top Dinantian depth map with the Agemar et al. 3D temperature model. Owing to the limited depth of the Agemar et al. model (max. 5000 m), a significant portion of the Top Dinantian temperature map is missing.

2.2.4 Belgium

2.2.4.1 Flanders

A 2D temperature map for Flanders and the Netherlands at the depth of the Dinantian was generated within the GeoHeatApp project (VITO et al. (2014), Figure 8a). This map was constructed by using a 28.1 °C/km gradient for the Cenozoic layers, and a 32.2 °C/km one for the older rocks. Within the Hotlime GeoERA project (Veldkamp et al. (2021) the Dutch part of the temperature map was updated by incorporating the Dinantian temperature from the SCAN project (Figure 8b). . Temperatures in the 2D map range from surface temperature to a maximum of ~200°C at the Dutch-Belgium border southeast of the Noord-Brabant province (NLD).

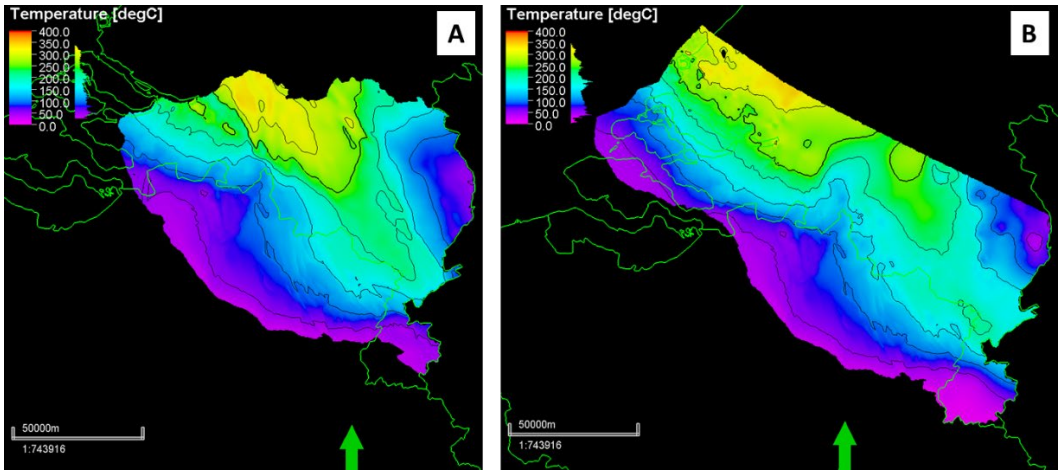

Figure 8 A. 2D grid of the temperature at the Top Dinantian compiled within the GeoHEAT-App project. B. 2D temperature grid at Top Dinantian compiled within the GeoERA Hotlime project. Contour interval 50°C. Note differences in a.o. the Ruhr Valley Graben area.

2.2.4.2 Wallonia

Well data with relevant information (e.g., location, depth, borehole temperature (BHT) measurements) are available for few wells within the lateral extend of the Dinantian in Wallonia (Figure 9). Data were supplied in tables in Excel format. The data listed in the Excel tables are based on Vandenberghe & Fock (1989), and complemented with more recent well data. Although Vandenberghe & Fock (1989) provided temperature distribution maps for Belgium (isotherms at depths of 500 m and 1000 – 5000 m), the maps lack the detail needed to calculate a 2D temperature gradient map. Therefore the original well data was used instead to calculate gradients for each well (see section 2.3).

Licour (2012) reported temperature measurements for wells in the vicinity of Saint-Ghislain, SW Wallonia. These temperature data appear to be similar to the data reported above. The gradients reported by Licour (2012) are discussed in the next section.

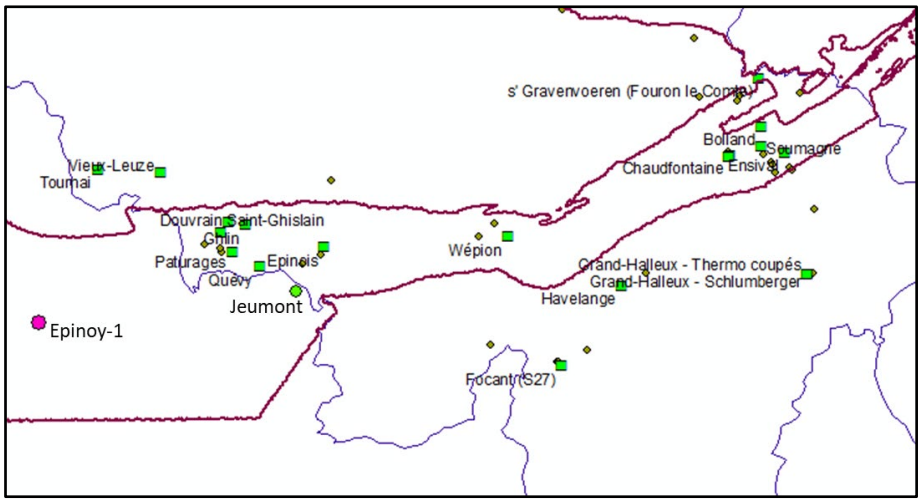

Figure 9 *Wells with borehole temperature data . Green squares: wells with temperature data received from SGB. Green circle: well Jeumont from Licour (2012). Purple circle: well Epinoy-1 from France (see France data section). Light green diamonds: other wells for which no temperature data is available.*

2.3 Map construction: Temperature gradient maps

2.3.1 Netherlands

A temperature gradient map is calculated for the Netherlands by dividing the Top Dinantian temperature map by the Top Dinantian depth map (Figure 10). Gradients for the Netherlands range between roughly 35 and 45 °C/km. Generally higher gradients (40-45°C/km) are observed NE of the Ruhr Valley Graben in the provinces of Gelderland and northern Limburg.

Three modifications were done on the gradient map at different stages during the gradient map construction phase. Firstly, the depth map has been modified by eliminating the grid cells where Z= 0 m. The depth map is referenced with respect to sea level, hence when dividing the temperature map by the depth map, cells in the depth grid that have 0 value (0m, sea level), return an error. This is particularly valid for the depth map in the region of south Limburg (blue ellipse, Figure 10). A second modification was applied to correct for negative gradients resulting from the fact that Petrel assigns negative values to depths below zero. Negative gradients were multiplied by -1 to return a positive gradient.

After initial calculation of the gradient map, it was observed that erroneously high gradients occur in the map (>50°C/km, see for example regions in the pink ellipses, Figure 10). These high gradients are caused by the fact that temperatures at or close to the surface show only minor variations (due to the models' grid size), while depth variations may be larger. For example, in areas where the Dinantian is at 100 or 200 m depth, and the temperature model predicts around 12°C, the resulting gradients are around 120°C/km and 60°C/km respectively. These gradients do not bear any geological meaning but are mere calculation artefacts. Therefore, as a final post-processing step, the gradient map has been modified by removing gradients >50°C/km.

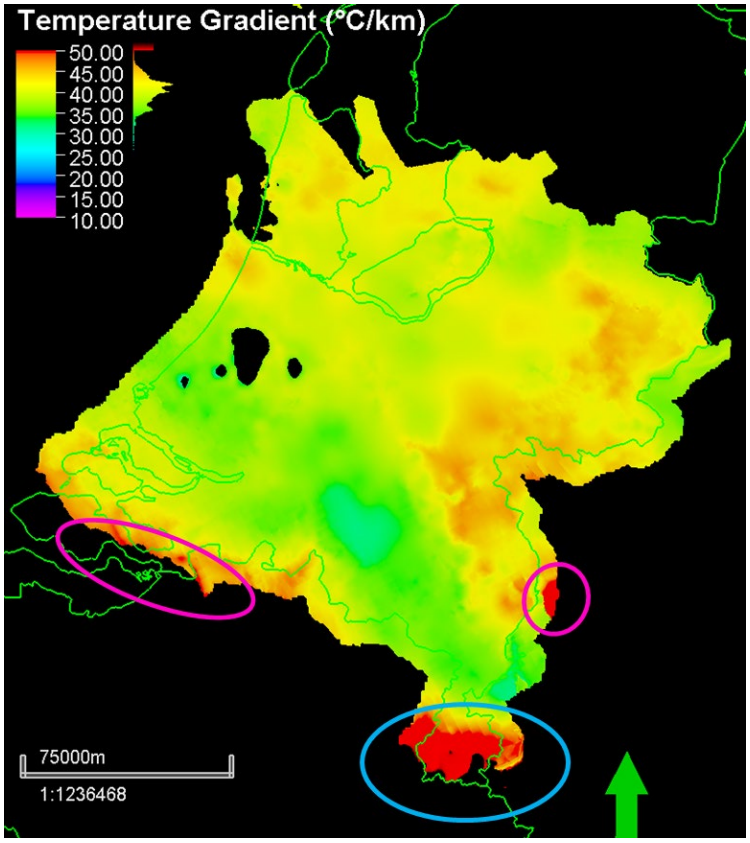

Figure 10 *Temperature gradient map for The Netherlands. Ellipses highlight areas for which the gradient is either erroneously high (pink) or calculated incorrectly (blue) due to the fact that Dinantian units are too close or at 0m elevation. See text for discussion. Data gaps in the province of South-Holland are due to the fact that the 3D temperature model does not extend beyond 10 km depth and the Dinantian is buried deeper.*

2.3.2 France

The BHT in well Epinoy-1 is 49.2 °C at the Namurian (at 785 m below surface) resulting in a high gradient of 49.9 °C/km (assuming a 10°C surface temperature).

The depth of the Dinantian at the site of this well is estimated at 4403 m below surface from the harmonised Top Dinantian depth map. This is significantly deeper than the Namurian interval from which the temperature was measured. A linear extrapolation of this gradient to the Dinantian is considered unreliable given that it is based on one well measurement, and it neglects conductivity changes in the varying lithologies between the Dinantian carbonates and Namurian shales.

Using the Bonté et al. (2013) temperature model is thought to be a better approach for deriving a gradient for northern France as this is based on a regional . The temperature profile at the location of Epinoy-1 well predicts a temperature at the Top Dinantian (4403 m depth) of 139.5°C based on the Bonté et al. (2013) temperature model (Figure 11). Assuming a surface temperature of 10°C, a gradient of 29.4 °C/km is obtained.

The calculated gradient at Epinois-01 is comparable to the gradient obtained for well Jeumont (see section Belgium data) and is therefore accepted as an adequate gradient estimate for Northern France. Because a simple extrapolation of one well would result in a large uncertainty range during contouring, a set of pseudo-wells (with gradients similar to the one calculated for Epinoy-1) are added during the gridding of the final gradient map (Figure 12).

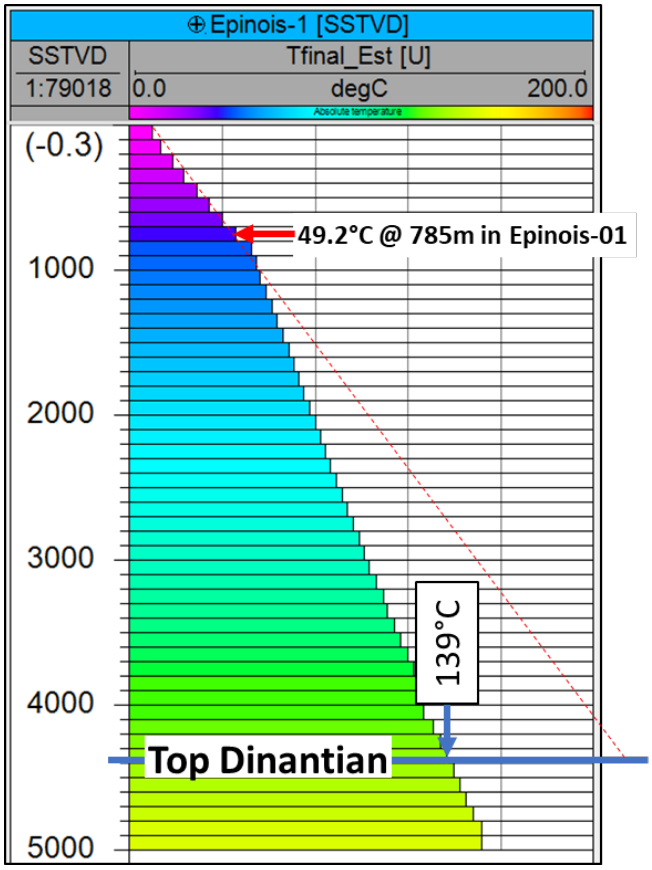

Figure 11 *Temperature profile for well Epinois-1 based on the Bonté et al (2013) temperature model. Temperature at the Top Dinantian (4403 m depth) is 139.5°C (blue arrow), resulting in a gradient of 30 °C/km (assuming a 10°C surface temperature). Red arrow indicates the borehole temperature in EPY-01 of 49.2°C at 785m depth. Thin dashed red line would be the gradient if a linear extrapolation from the EPY-01 borehole temperature to the depth of the Dinantian would be applied (resulting in a too high temperature estimate).*

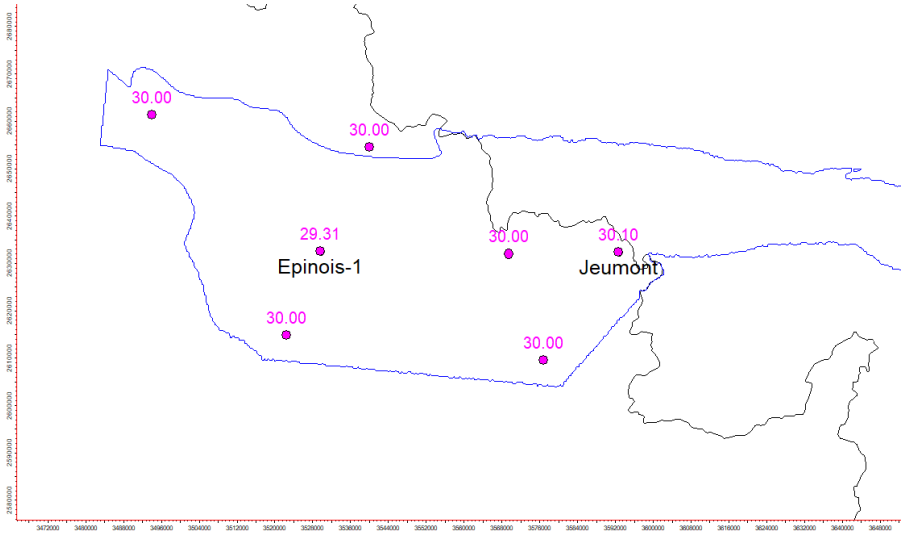

Figure 12 *Map showing calculated gradients (°C/km) for wells Epinois-1 and Jeumont (for the latter, see Belgium data section). Pseudo-wells (points without names) are added to aid the kriging process when constructing the final 2D gradient map. Blue line indicates the extend of the Top Dinantian.*

2.3.3 Belgium

2.3.3.1 Flanders

The temperature gradient map for the Flanders region is calculated from the Hotlime GeoERA Top Dinantian temperature map and the DGE Rollout harmonised Top Dinantian depth map (Figure 13). Similar modifications have been applied as have been discussed for the gradient map in the Netherlands (see section 2.3.1 for discussion on modifications): depths where Z=0 m have been removed from the depth map, and erroneously high gradients (>50 °C/km) have been removed as a post-processing step after calculating the final gradient map.

Clearly visible from the gradient map is that for the Dutch part, the gradients vary in the 2D grid (as they are based on the SCAN 3D temperature model). For the Flanders part, however, a nearly uniform gradient of about 35 – 38 °C/km is observed.

Given that the temperature distribution in the Flanders region is not accurately known, it is argued that using the detailed 2D gradient map does not result in a more accurate gradient map. Hence, for the Flanders region, a 5x5 km wide grid was constructed and a (simplified) uniform gradient of 37°C/km gradient is assigned to all grid nodes (Figure 14).

To check if this 37°C/km gradient is acceptable, the gradient is used to predict the temperature at the Top Dinantian at the site of the Balmatt deep geothermal well (MOL-GT-01, Laenen et al., 2014; Bos et al., 2018). The Top Dinantian at this site is found at 3170 m depth and using the 37°C/km gradient predicts a temperature of ~117°C. This is in close agreement with reported production water temperatures of 128°C from MOL-GT-01 (Bos et al., 2018).

We therefore consider using a constant gradient of 3°C7/km as acceptable for Flanders. To accommodate transitions from the Flanders region towards the gradient map for the Netherlands, an ~25 km buffer zone is adopted (Figure 14).

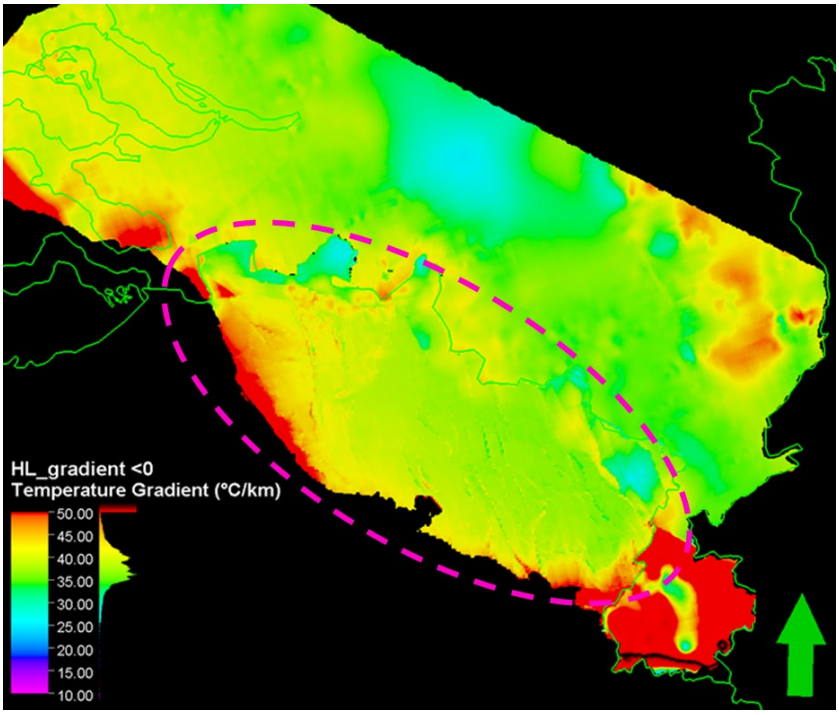

Figure 13 Temperature gradient map calculated from the Hotlime GeoERA temperature map (Veldkamp et al, 2021) and the DGE Rollout harmonised Top Dinantian depth map. Clearly visible is the transition in gradients from Flanders (uniform gradient) to the Netherlands (SCAN 3D model gradient), purple ellipse.

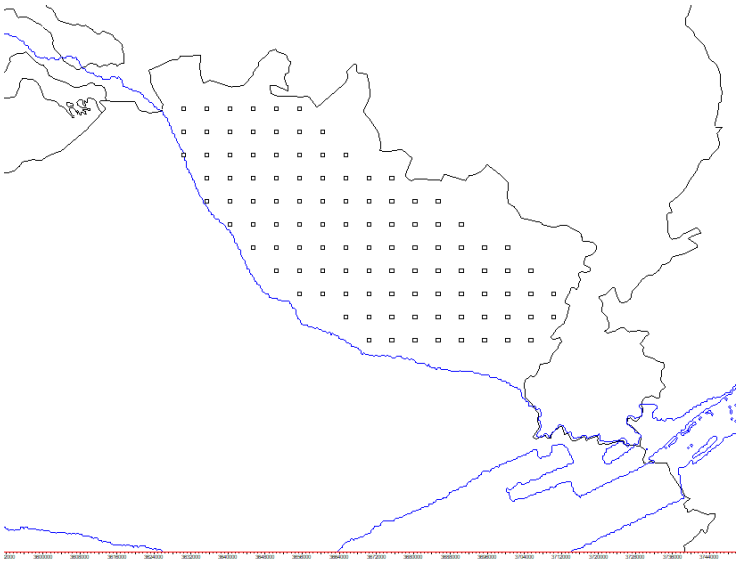

Figure 14 An 5x5 km grid with a constant gradient of 37°C/km is constructed as input for the regional Dinantian gradient map. An ~25 km buffer zone is adopted between the Flanders grid and the Dutch gradient map to accommodate temperature gradient transitions.

2.3.3.2 Wallonia

BHT data are used to calculate a temperature gradient for each available well location (Figure 15 and Table 1). A simple, linear data regression is calculated through the data, assuming a 10°C surface temperature (e.g. Wépion, Figure 15A). For wells that have very limited BHT (one or two temperature measurements, e.g. Paturages, Figure 15B), the regression is a simple linear fit from the BHT data point to 10°C surface temperature. Appendix A provides all available BHT data. Although all

calculated gradients are reported in Table 1 only the wells that lie within the lateral extend of the Dinantian in Wallonia have been used when gridding the regional temperature gradient map.

Licour (2012) calculated gradients for a selected number of wells (Table 1). Because of small differences between the Licour (2012) and the present data, and to maintain data consistency, the gradients calculated from the original SGB Excel data tables are used to compile the Top Dinantian temperature map. One well with BHT not reported in the SGB Excel sheet (well Jeumont, see also section 2.3.2) was manually added from the georeferenced map in Licour (2012).

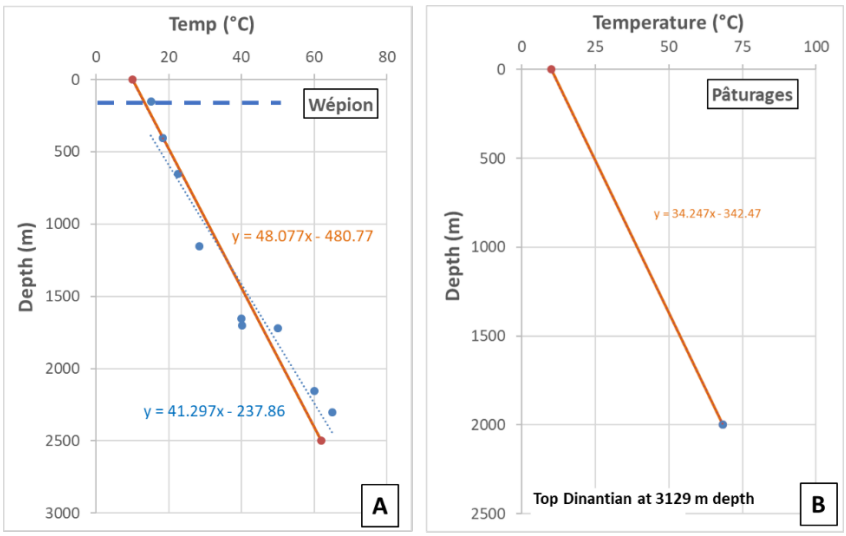

Figure 15 *Examples of borehole temperature (BHT) data (blue circles) from Wallonia for locality Wépion (A.) and Paturages (B.). Blue dotted line represents a simple, linear data regression; orange solid line is data regression for a 10°C surface temperature. The latter is used to calculate the temperature gradient. Some wells have abundant BHT data (e. Wépion), whereas others have limited BHT data (e.g. Paturages). Depth of Top Dinantian in Wépion (177 m) is indicated by the thick dashed blue line; for Paturages, the depth is at 3129 m.*

Table 1 *Well data with BHT and calculated gradients for Wallonia.*

Well	X LAMBERT 2005	Y LAMBERT 2005	AREA	ALTITUDE	Depth (TD, m below surface)	Depth Top Dinantian (m below surface)	Calculated temperature gradient (°C/km)	Temperature gradient (°C/km) - Licour (2012)
Havelange	212583.18	110294.20	Ardennes	286	5648	no grid	20.3	28.0
Grand-Halleux - Thermo coupés	259432.91	112220.90	Ardennes	321	3225	no grid	18.4	
Grand-Halleux - Schlumberger	259432.91	112220.90	Ardennes	321	3225	no grid	19.9	
Focant (S27)	196838.00	90400.00	Ardennes	139	3208	no grid		
Wépion	183951.74	123412.91	Ardennes	153	2310	178	26.1	23.9
Martouzin Neuville	no coordinates		Ardennes				26.1	
Saint-Ghislain	111626.70	126269.22	Hainaut (Mons Basin)	26	5403	2008	32.3	31.9
Tournai	80832.50	143148.70	Hainaut (Mons Basin)	47	1271	no grid	29.8	28.9
Quévy	121063.00	117419.00	Hainaut (Mons Basin)	76	1345	2962	18.2	29.0
Vieux-Leuze	96822.20	141907.80	Hainaut (Mons Basin)	49	1536	no grid	24.7	24.0
Douvrain	113597.75	129095.45	Hainaut (Mons Basin)	31	1447	1119	43.4	
Epinois	137539.75	122014.59	Hainaut (Mons Basin)	128	2009	2254	23.5	23.0
Ghlin	117670.48	128153.44	Hainaut (Mons Basin)	29	1579	1308	38.6	
Paturages	114212.49	121529.51	Hainaut (Mons Basin)	101	2000	3130	29.7	29.2
Baudour	no coordinates		Hainaut (Mons Basin)				31.6	
Tilleur	no coordinates		Liege				30.0	
Val Benoit	no coordinates		Liege				41.5	
Soumagne	248472.95	144713.24	Herve	257	2528	1202	19.7	
Bolland	248618.10	149817.40	Herve	278	3001	503	22.0	
Chaudfontaine	240614.00	142570.00	Herve	80	1229	633		
Chaudfontaine1 - Schlumberger	240262.00	142367.00	Herve	80	548	611	33.7	
Chaudfontaine1 - 1966	240262.00	142367.00	Herve	80	548	611	33.7	
Chaudfontaine (sources)	no coordinates		Herve					
Ensival	254442.00	142922.00	Herve	150	1020	741	31.4	
s' Gravenvoeren (Fouron le Comte)	248486.00	161971.00	unknown	96	866	48		
134E318			unknown					
Licour (2012 data not in SGB Excel table								
Jeumont	no coordinates							30.1

2.3.4 North Rhine-Westphalia

2D Temperature gradient maps for the NRW region have been calculated from the 3D Arndt and Agemar et al (2012) temperature models (Figure 16). Similar modifications have been applied as have

been discussed for the gradient map in the Netherlands (see section 2.3.1 for discussion): depths where Z=0 m have been removed from the depth map, and erroneously high gradients (>50 °C/km) have been removed as a post-processing step after calculating the final gradient map.

Temperature gradient maps for both data sets show a fairly consistent gradient of ~31-33°C/km (Arndt dataset) and ~36-38°C (Agemar dataset). This shows that the original temperature maps were constructed using a uniform gradient, likely due to the absence of detailed temperature information.

When comparing the temperature gradients in the border region between NRW and the Netherlands, it is observed that the gradient calculated from the Agemar model is similar to the Dutch gradients (Figure 10). The gradient calculated from the Arndt temperature model is lower. For calculating the cross-border gradient map, the Agemar gradient is preferred.

Given that the temperature distribution in the NRW region is not accurately known, a similar approach is adopted as for the Flanders region. A 10x10 km wide grid was constructed and all grid nodes are assigned a 37°C/km gradient derived from the Agemar temperature model (Figure 17). To accommodate a smooth gradient transition from the NRW region to the Dutch border, an ~25 km buffer zone is adopted.

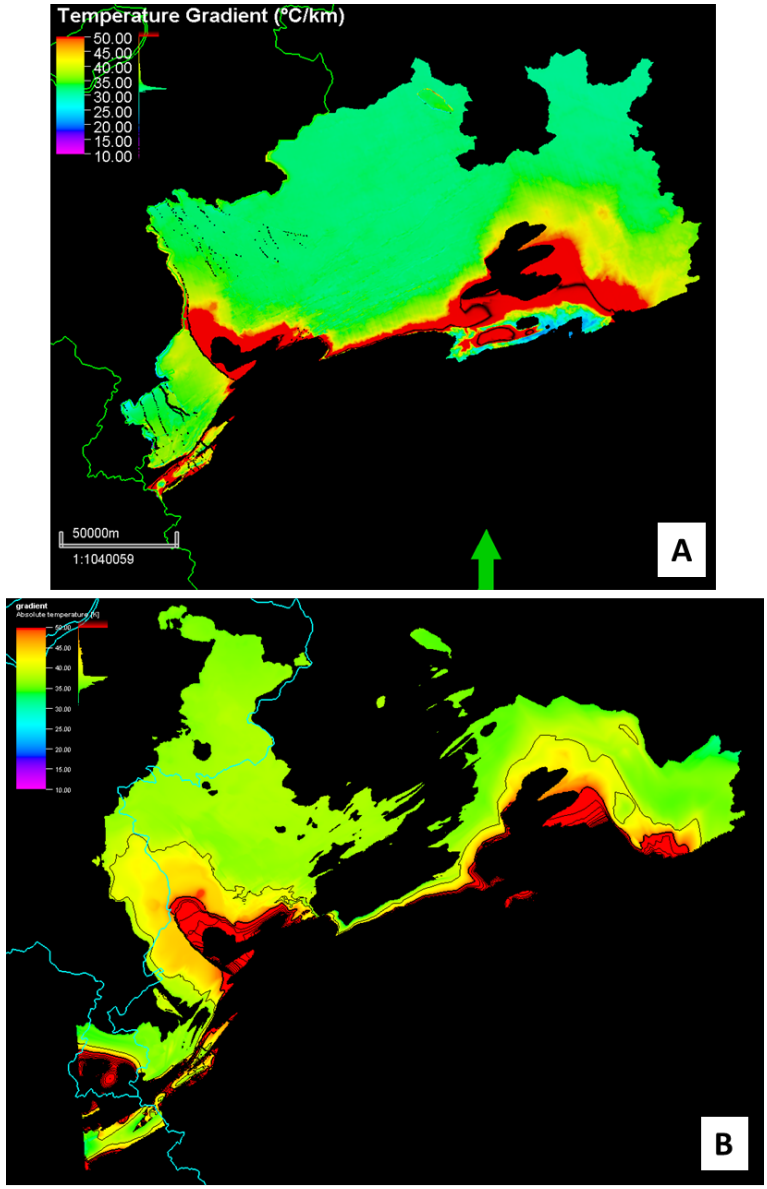

Figure 16 Temperature gradient maps for North Rhine-Westphalia. A. Gradient calculated from the Top Dinantian temperature dataset provided by M. Arndt. B. Temperature gradient calculated from the Agemar temperature model (Agemar eta al., 2012). For both models, a rather constant gradient of ~31-33°C/km (Arndt model) and 36-38°C (Agemar model) are calculated.

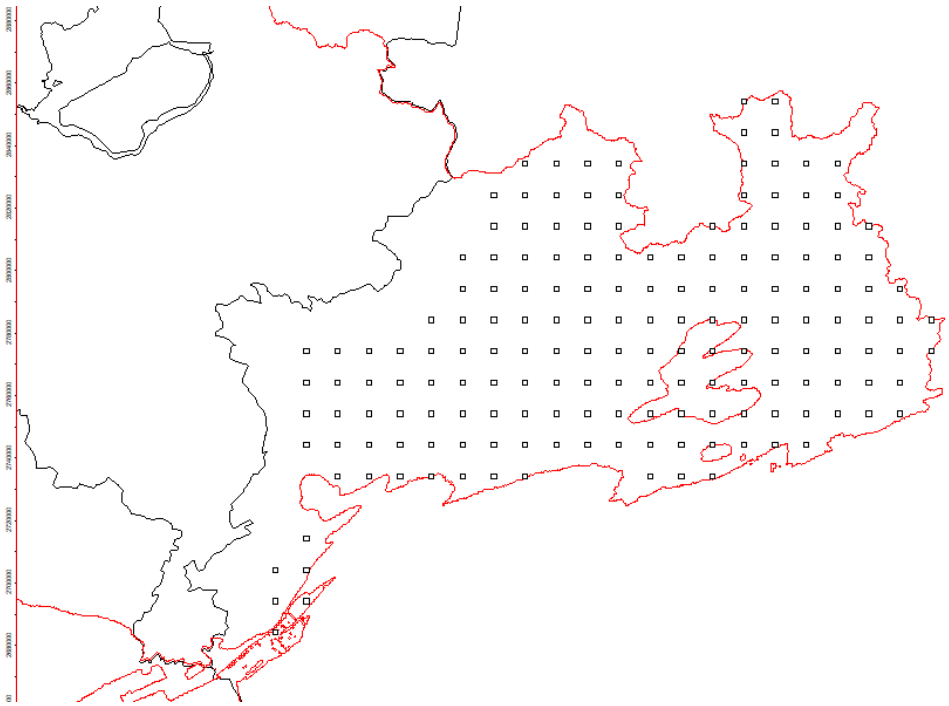

Figure 17 An 10x10 km grid with a constant gradient of 37°C/km is constructed as input for the cross border Dinantian gradient map. An ~25 km buffer zone is adopted between the Dutch border and the NRW grid to accommodate temperature gradient transitions.

2.4 Cross border gradient and Top Dinantian temperature maps

From the calculated gradients (2D maps, well data, grids) a cross border gradient map was compiled in Petrel using convergent gridding (Figure 18 and Figure 19). Gridding was allowed within the lateral extend of the Top Dinantian depth map (blue line in Figure 18) and tolerance was set to 5% for minimum gradient (26°C/km) and 20% for the maximum gradient (45°C/km). Grid resolution is 250x250m.

The gradient transitions between the Dutch and Flanders and NRW borders are generally rather smooth. However, owing to the use of a constant gradient for both Flanders and NRW, rapid gradient transitions are observed east of the Dutch province Zeeland towards the Flanders part as well as into Germany. Here future fine-tuning and incorporating new temperature data from future drilling projects will improve the gradient map.

The final Top Dinantian temperature map is calculated as (Figure 20):

Temperature_Top Dinantian = Temperature gradient * Depth_Top Dinantian + 10°C

Calculated temperatures for the Top Dinantian range from surface temperature in areas where it is outcropping to maximum values around 400-450°C in the Dutch West Netherlands Basin. In the northern NRW region, maximum temperatures reach roughly 350°C.

Temperature information from two deep geothermal wells drilled into the Dinantian are used to test the temperatures in the Top Dinantian temperature map. The California geothermal well CAL-GT-01 (Venlo, Limburg, The Netherlands) encounters the Top Dinantian at a depth of 1635 m. Reported production water temperatures range from 77.6°C to 80.4°C (VITO, 2012). The temperature at this

location predicted from the new temperature map (Figure 20) is 65-70°C, which is slightly lower, but in close agreement with the production water temperature from CAL-GT-01.

In the Balmatt deep geothermal well near Mol in Flanders), the Top Dinantian is encountered at a depth of 3170m and reported production water temperatures are 128°C (Bos et al., 2018). From the new Top Dinantian temperature map, it is predicted that the Dinantian should have a temperature of 120-125°C, which is in good agreement with the reported well temperature data.

2.5 Concluding remarks on the Top Dinantian temperature map

The new Top Dinantian temperature map provides a first assessment and prediction of the temperature distribution of the Top Dinantian in the wider Dutch, Belgian, German and northern France regions. Cross checking the predicted temperatures with measured temperatures from production water in two deep geothermal wells in the Netherlands and Flanders shows a good fit, suggesting that at least regional trends in temperature distribution are well captured.

However, the Top Dinantian temperature map was constructed using several assumptions and simplifications. Fine-tuning and incorporating new temperature data from future drilling projects will improve the temperature map.

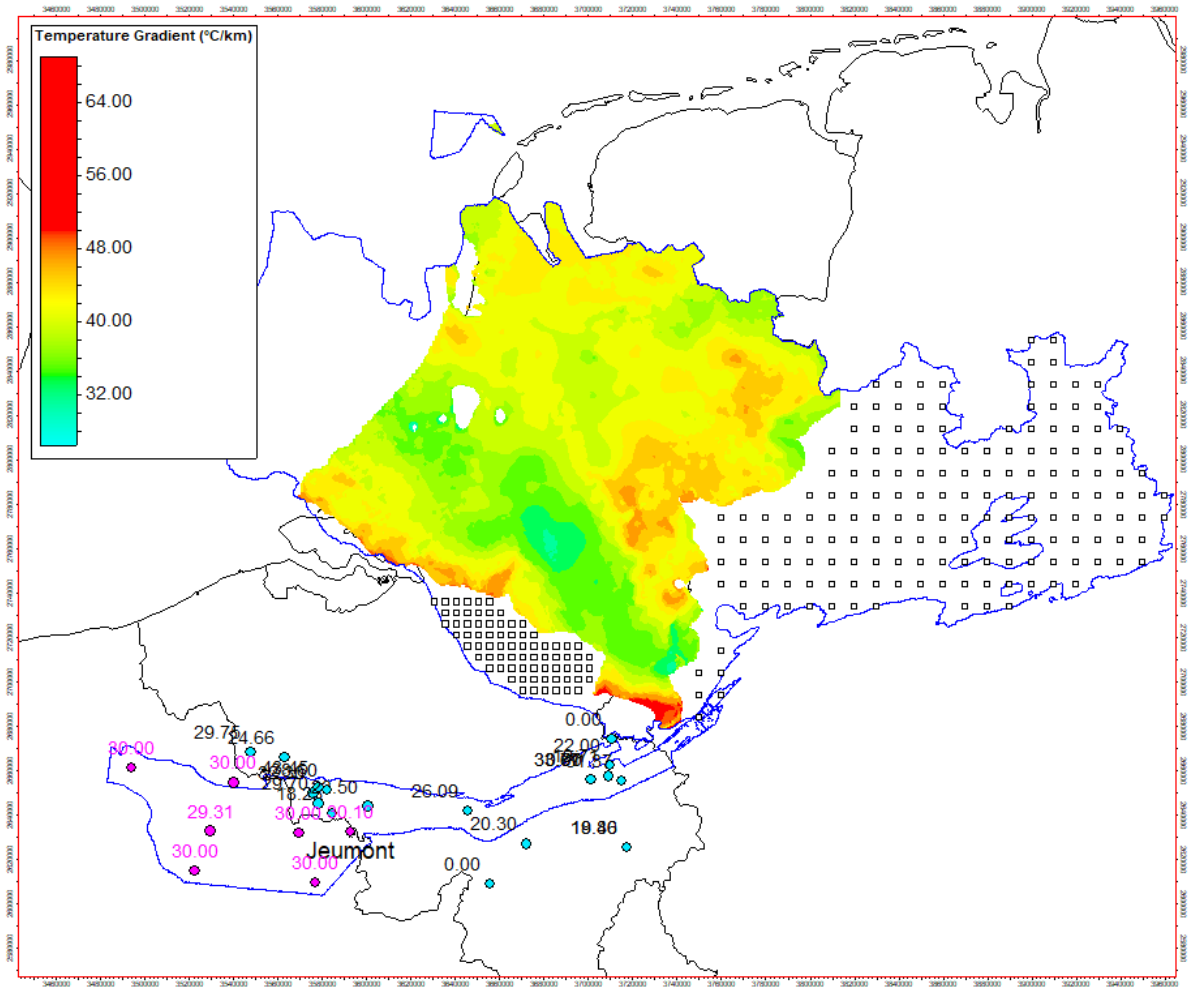

Figure 18 Input data used to calculate the cross-border temperature gradient map. For data sources see section XXX. Blue line depicts the lateral extend of the harmonised Top Dinantian depth map.

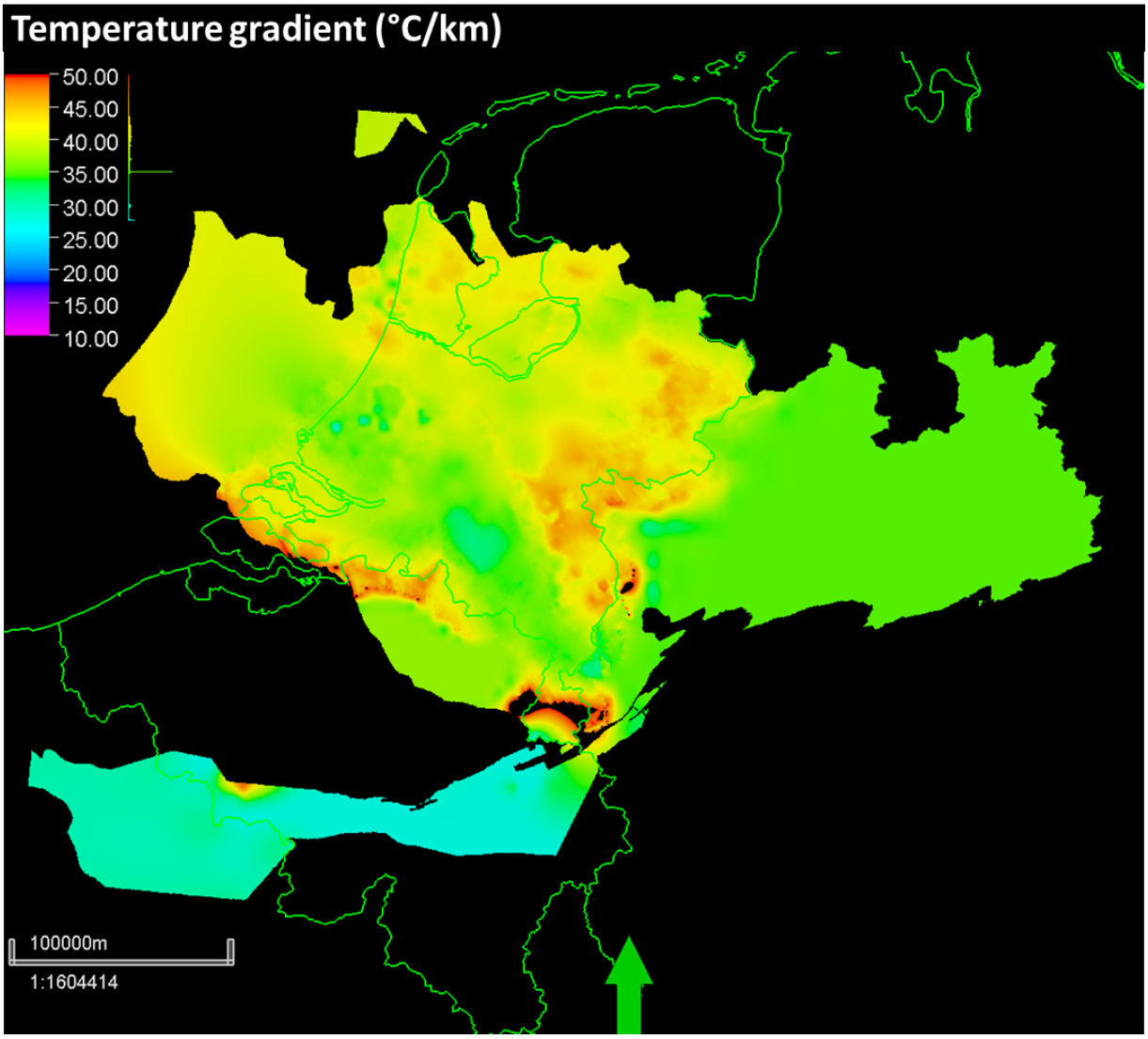

Figure 19 Calculated cross-border gradient map.

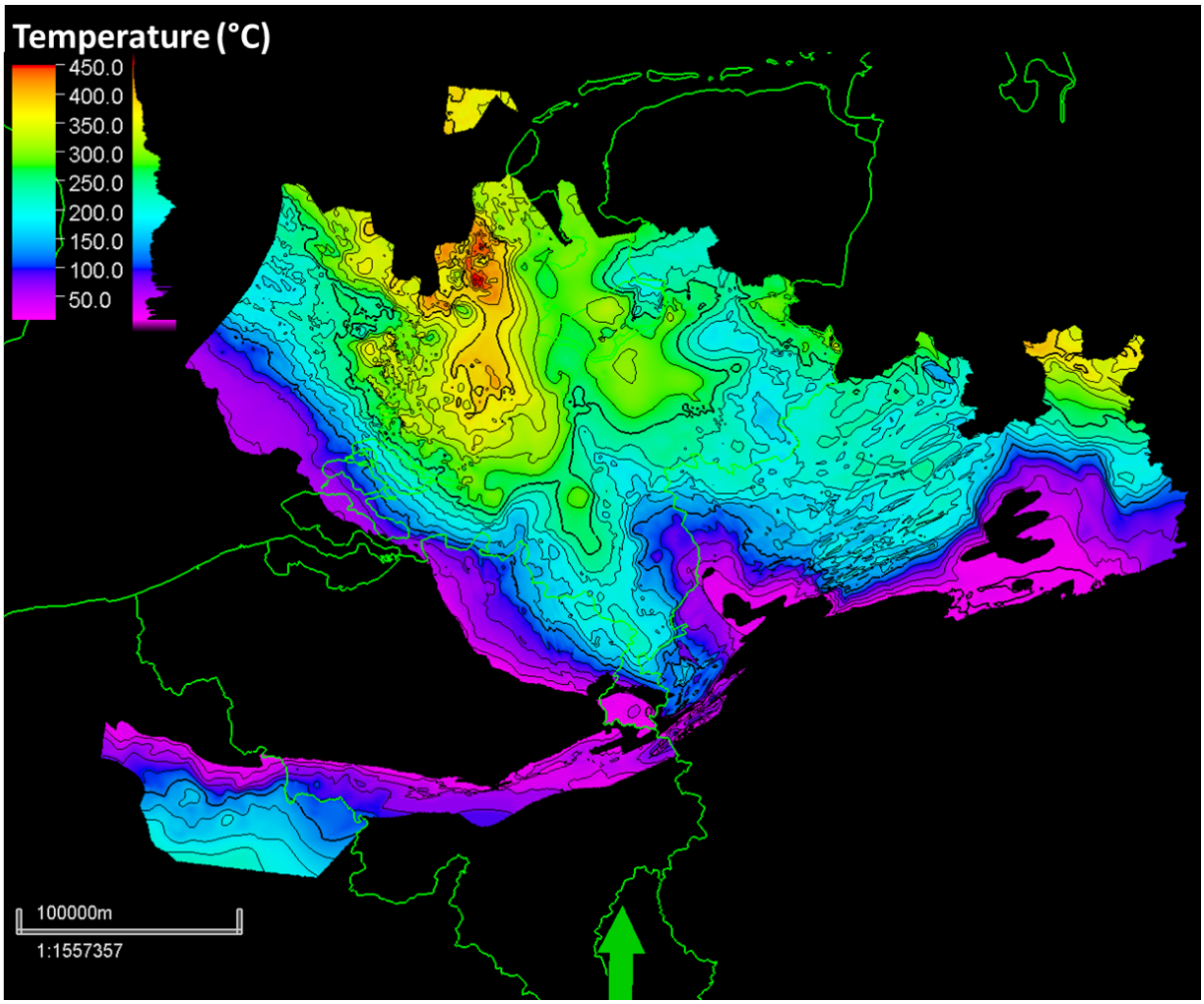

*Figure 20 Calculated temperature map for the Top Dinantian. Temperature_Top Dinantian = Temperature gradient * Depth_Top Dinantian + 10°C.*

3 Permeability

3.1 Previous studies

Various previous projects studied the Dinantian in relation to its geothermal potential. The most relevant for the current study are GeoHeat-APP, UDG SCAN, GeoERA HotLime and GeoERA Hike.

GeoHeat-APP studied the economic feasibility of intermediate and deep geothermal for a sustainable heat demand of construction and renovation projects in Flanders and the southern Netherlands (VITO et al. (2014)). During this project, depth and temperature maps of the Dinantian were generated, and a map which shows areas with increased geothermal potential in faults in Dinantian rocks in the classes 'possible', 'medium' and 'high potential'.

The SCAN Dinantian project focused, among other topics, on characterization of the Dinantian in the Netherlands. The facies, petrophysics and the fracture distribution and density in the Dinantian in the Netherlands was analysed in detail (Carlson (2019); Mozafari et al. (2019); Van Leverink & Geel (2019)). As part of the project the following recommendations for future work if one were made to assess the geothermal potential of the Dinantian:

- Probability of the presence of fracture corridors;
- Probability of the presence of open fractures (e.g. due to recent tectonic activity);
- Probability of the presence of open fractures due to their orientation parallel to the maximum horizontal stress direction;
- Probability of the presence of a geomechanical facies favourable for the formation of fractures

These maps could then be combined with maps from other datatypes and disciplines:

- Curvature maps, indicating different degrees of folding of the strata
- Probability of the presence of karst
- Probability of matrix porosity & permeability

The GeoERA project HotLime project focused on mapping and assessment of geothermal plays in deep carbonate rocks. For the Netherlands, the Dinantian was chosen as pilot area. HotLime WP2 investigated the potential evaluation of carbonate aquifers (Veldkamp et al. (2021)).

Finally, the GeoERA HIKE project aimed at "supporting research and assessments of induced hazards and impacts that are related to the exploitation of subsurface resources and capacities throughout Europe", to "be achieved through development, demonstration and implementation of harmonized subsurface data sets and methodologies, investigation of applied use cases, and facilitation of knowledge shared between geological surveys and stakeholders. One of its work packages focused on the development of a European fault database which was used in the current project (ten Veen (editor) (2021)).

It is acknowledged that the exact location of the HIKE faults at the level of the Dinantian is uncertain when the aquifer is buried deeply. Not only were not all faults mapped down to Dinantian level but extrapolated downward which introduces a location error, but it is also uncertain how far presumed faults extend downward, and whether they extend in a true vertical direction, or are listric. For near vertical faults at the mapping depth, one may assume a vertical prolongation, but for the thrust-like faults encountered in Wallonia and northern France, this is problematic.

3.2 Factors influencing the permeability

In the context of the permeability assessment, special focus was put on the impact of fault and fracture permeability. According to the analysis in the SCAN Dinantien project (van Leverink & Geel, 2019), the matrix permeability of the Dinantian carbonates is very low and significant flow potential can only be generated from fracture permeability. The Dinantian carbonates in the study area can therefore be classified as a Type 1 fractured aquifer as described by Sun & Pollitt (2021).

Table 2 Fractured aquifer classification into Type 1, Type 2 and Type 3 with characteristics, lithology, matrix and fracture properties and range of ultimate recovery factors (Sun & Pollitt (2021))

classif-ication	characteristics	lithology	matrix properties	fracture properties	ultimate oil recovery factor
Type 1	Tight matrix: fractures and solution-enhanced fracture porosity provide both storage capacity and fluid-flow pathways	Basement, dolomite and limestone	Negligible matrix porosity and permeability	Bulk porosity ranges from 0.8–5.8% (average 3.2%); well test permeability average 184 mD (maximum 3700 mD)	Range from 13–55% (average 31%)
Type 2	Macroporous matrix provides the primary storage capacity while fractures and solution-enhanced fracture porosity provide essential fluid-flow pathways	Limestone, dolomite, sandstone and volcanics	Porosity ranges from 4–20% (average 11%); air permeability average 5 mD (maximum 100 mD)	Fracture porosity ranges from 0.1–1.5% (average 0.95%); well test permeability average 103 mD (maximum 3280 mD)	Range from 7–65% (average 35%)
Type 3	Microporous matrix provides all storage capacity while fractures only provide essential fluid-flow pathways	Chalk, chalky limestone, diatomite, chert and siltstone	Porosity ranges from 5 to 34% (average 20%); air permeability average 2 mD (maximum 5 mD)	Fracture porosity ranges from 0.1–2% (average 0.9%); well test permeability average 62 mD (maximum 1800 mD)	Range from 8–57% (average 30%)

The main factors that influence the permeability of the Lower Carboniferous in the study area were therefore:

Fault permeability

- Fault type
- Fault length
- Fault displacement
- Damage zone width
- Fracture intensity
- Fault direction with respect to the stress field direction
- Recent fault activity
- Fault dip
- Bed thickness

Karst permeability

- Subaerial exposure
- Depositional facies
- Water circulation

Matrix permeability

- Burial history/depth
- Depositional facies
- Diagenesis

In the following sections the assumptions and workflows for these factors are discussed in detail.

3.3 Matrix permeability

As described earlier the matrix permeability of the Dinantian carbonates is very low. Only areas affected by dolomitization show a higher permeability (Mozafari et al. (2019)). However, areas affected by dolomitization are very unevenly distributed and show no clear trend that would allow a regional interpretation of higher poro-perm domains related to dolomitized carbonates. The effect of diagenesis and burial history on the facies and petrophysical properties of the Dinantian is described in detail in Mozafari et al. (2019). In the context of their study no clear trend between facies, depositional environment, and burial history could be identified that would allow to extrapolate the petrophysical properties of the Dinantian carbonates. It was therefore decided to use average permeability values for the different general depositional facies, identified by Mozafari et al. (2019), Figure 21), as described by Bruijnen (2019).

Table 3 Matrix permeability assignment for the maximum, average and minimum case based on the lithofacies classification from Mozafari et al. (2019) and the petrophysical evaluation from Carlson (2019) compared to the values used by Bruijnen (2019).

	Matrix porosity (%) (Bruijnen (2019))	Matrix permeability (mD) (Bruijnen (2019))		Max matrix permeability (mD)	Avg matrix permeability (mD)	Min matrix permeability (mD)
Dolomite	4	8	-			
Platform	5	1	Platform carbonates (unc pres + outline)	1	0.4	0.1
			Platform carbonates (unc outline)	1	0.4	0.1
			Platform carbonates	1	0.4	0.1
Basinal carbonate	0.5	0.1	Basinal deposits	0.4	0.1	0.1
			Possible basinal structural high	0.4	0.1	0.1
			Basinal high	0.4	0.1	0.1
Basinal shale	0	0	Kulm facies	0.001	0.001	0.001

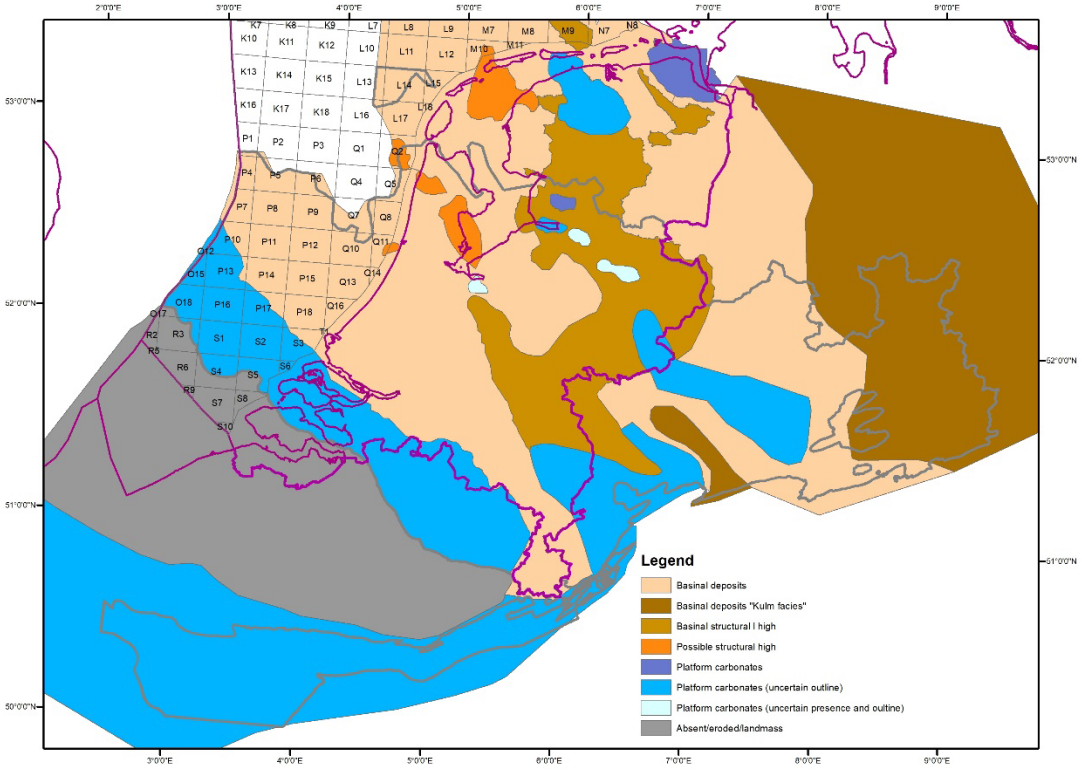

Figure 21 Facies distribution map for the Visean showing the distribution of the depositional environment and carbonate platforms based on the results of the SCAN study (Mozafari et al. (2019)), extended towards Germany, Belgium and France by the facies map published in the Interreg Mid-Term report (Fritschle et al. 2021). The grey line represents the outline of the mapped area.

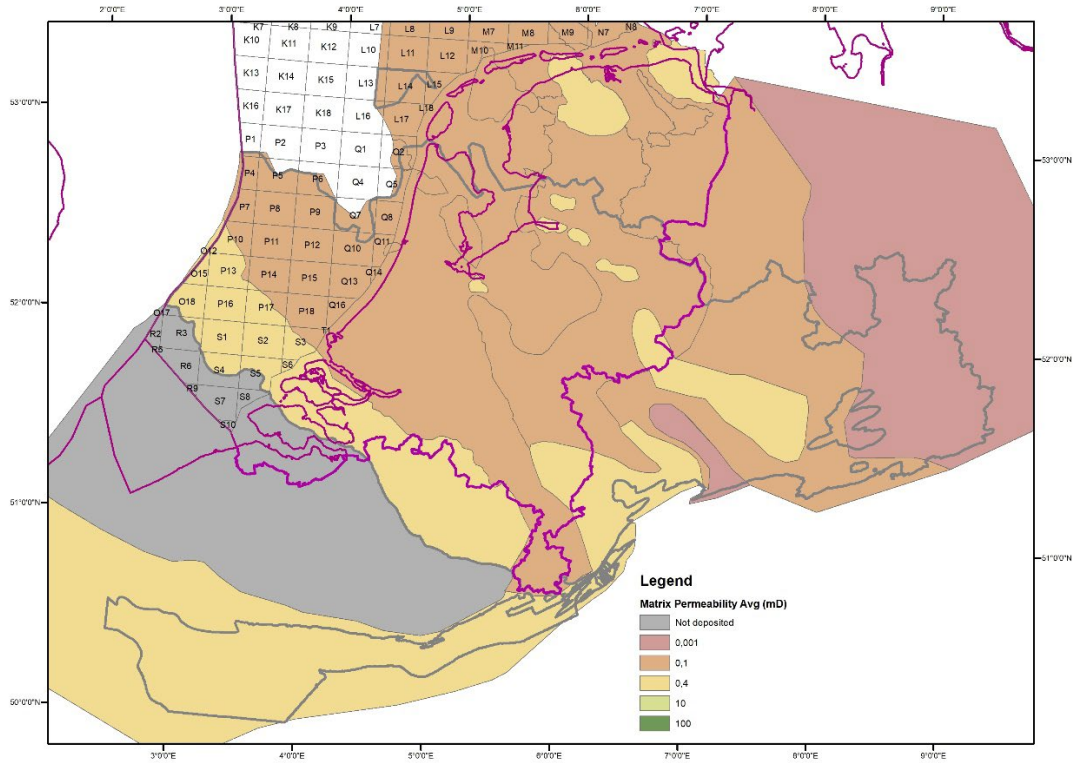

Figure 22 Map for the average case for the matrix permeability as defined by Table 3 and Figure 21. The grey line represents the outline of the mapped area.

3.4 Karst permeability

During the SCAN UDG project the processes and areas affected by karstification related to dissolution by groundwater influences were assessed for the Dutch subsurface. In this study, three main phases of karstification were identified, intra-Dinantian, end of Dinantian (Carboniferous) and intra-Cretaceous. The intra-Dinantian proved to be difficult to map, while the areas affected by the other two phases were mapped (Figure 23) for the SCAN study area (Dutch onshore and north-eastern part of Belgium). A detailed overview of the processes of karstification, the definition as well as potential karst fillings and their effect on the porosity and permeability of the Dinantian is given in Mozafari et al. (2019). In addition to these phases of paleo-karstification, the present-day karstification in areas influenced by present-day ground water flow can also play a role in the study area. Areas with a top elevation above 0 m as well as areas above a top depth of 100 m were selected and also included into potentially karst-influenced areas (Figure 23).

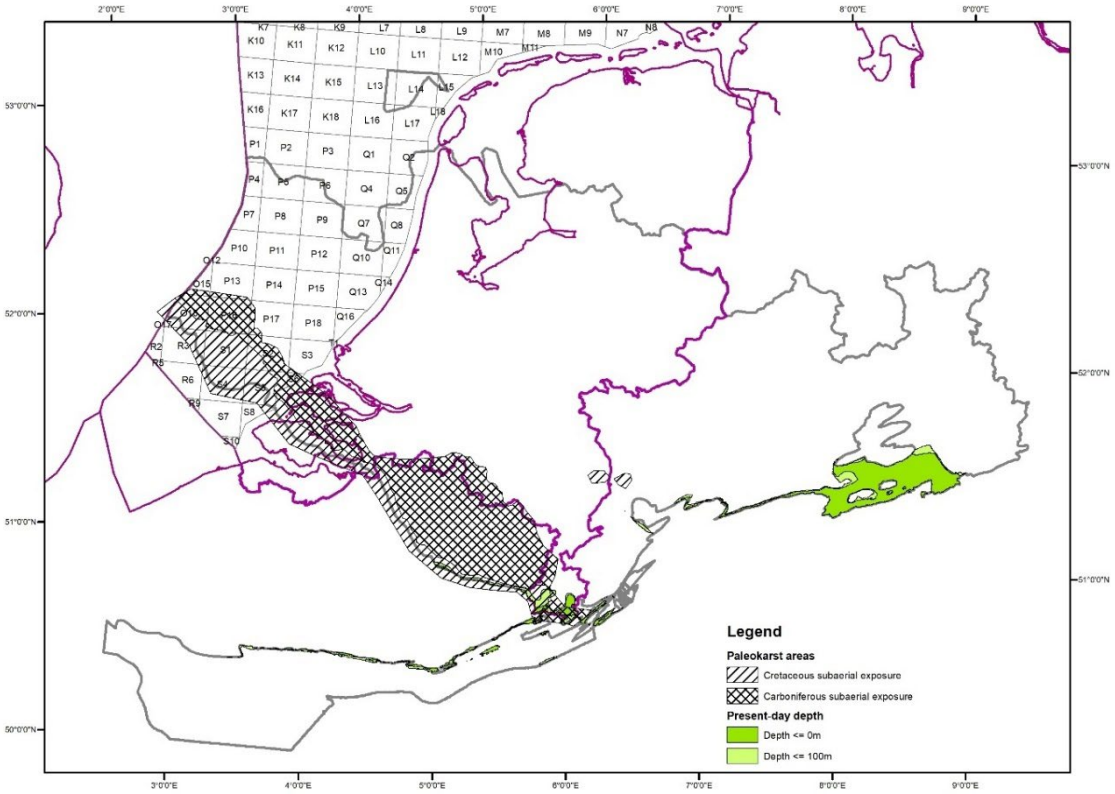

Figure 23 Areas with potential karst features based on the SCAN results (Mozafari et al. 2019) and the present-day depth map (this report)

To account for additional permeability related to karst features, an overall higher permeability was assigned to the areas with known potential for karst. The karst features related to the Intra-Cretaceous karstification were described to be more pronounced compared to the Carboniferous karstification. Also, areas at present-day located above 0 m elevation also have a higher possibility for karstification, compared with areas between 0 and 100 m depth. An overall higher matrix permeability was assigned to these areas as described in Table 4.

Table 4 Assumptions for minimum, average and maximum matrix permeability in areas affected by karstification for the different phases.

Karstification phase	Minimum case	Average case	Maximum case
Intra-Cretaceous	No change from base case	100 mD	1000 mD
Carboniferous		10 mD	100 mD
Present-day 0 m		100 mD	1000 mD
Present-day 100 m		10 mD	100 mD

During the SCAN project no clear link could be identified between the degree of karstification and the depositional setting. Figure 24 shows the resulting background permeability distribution for the average case accounting for higher permeabilities in karstified areas.

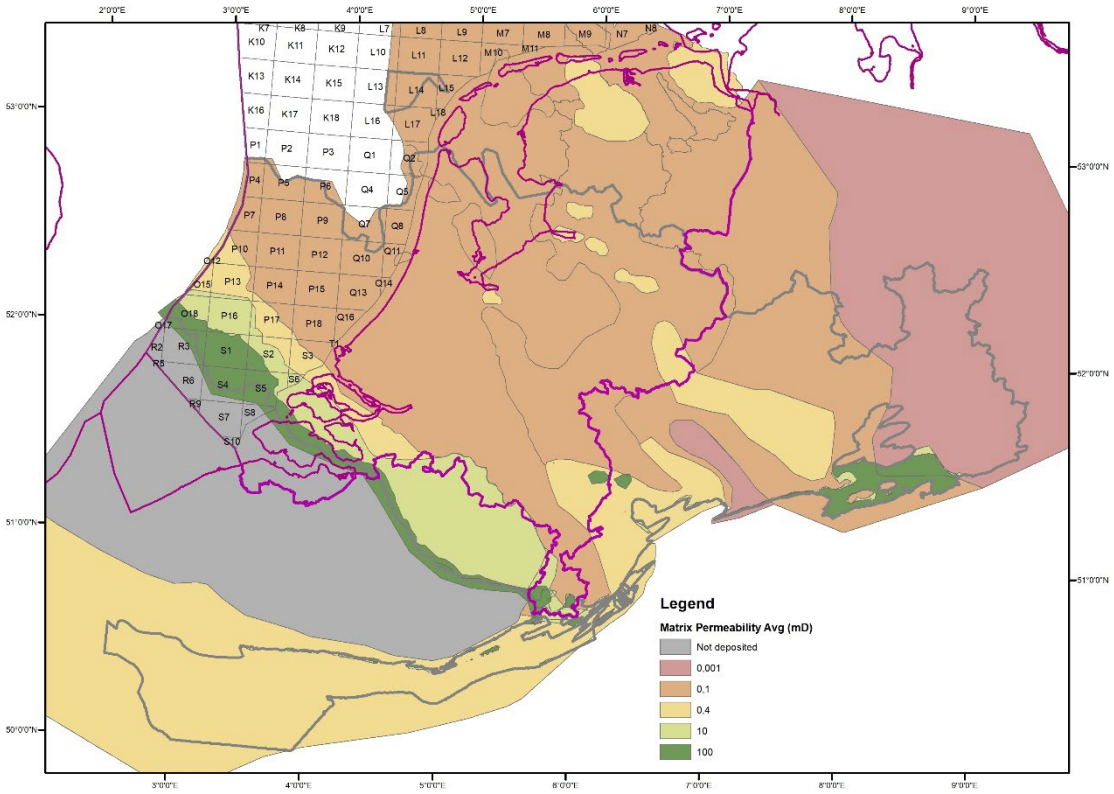

Figure 24 Matrix permeability including areas affected by karstification for the average case

3.5 Fracture permeability

Fracture permeability together with karstification processes have been identified to affect the permeability of the Dinantian carbonates the most. Since fracture systems are difficult to assess on seismic, it was attempted to use larger faults as an indication for the level of fracturing. Therefore, in order to assess areas with good potential for fault related fracture domains the newly compiled pan-European Hike fault database was used to identify strongly faulted and potentially fractures areas (ten Veen (editor) (2021).

In the Hike dataset the fault trace location as well as total trace length was available for all faults in the study area. Additional information such as fault type (normal, reverse, strike-slip or inverted, see ten Veen, 2021 for details), fault dip, fault displacement or fault direction was available for most of the faults in the area.

The different countries use different approaches to identify the main interval intersected by the respective fault. The dataset for the Netherlands includes the youngest and oldest intersected stratigraphic level as well as the reference level (stratigraphic unit the fault transects at the mapped location) for the fault trace for most of the faults. However, the oldest unit included in the dataset is the base Permian. The French dataset did not include stratigraphic information, the data from Belgium and Germany includes information on the reference levels of some faults with the oldest available interval being the Carboniferous and Permian respectively.

For all countries the faults intersecting the oldest stratigraphic intervals as well as the faults without stratigraphic information were selected, cropped to the extent of the area of interest and duplicates removed.

3.5.1 Fault length and fault displacement

Several authors have linked the extent to which a fault has fractures to the surrounding rock and the magnitude of fault displacement (e.g., Bense et al. (2013); Childs et al. (2009); Choi et al. (2015) and references therein). Even though this value varies along the fault, it was decided to use a correlation between average fault displacement and damage zone width (Choi et al. (2015)) to be able to get an indication of the lateral extent of potential fracturing. Since only a limited number of faults in the HIKE database were given an average fault displacement value, the correlation between fault length and displacement published by Kim & Sanderson (2005) was used to calculate an indication of possible fault displacement. Kim & Sanderson (2005) identified different correlations based on the type of fault (normal faults, thrust faults, strike-slip faults, Figure 25) which were individually used for the calculation. The available data from the HIKE database that contained both fault length and displacement was used to calibrate the correlation for normal faults (Figure 26).

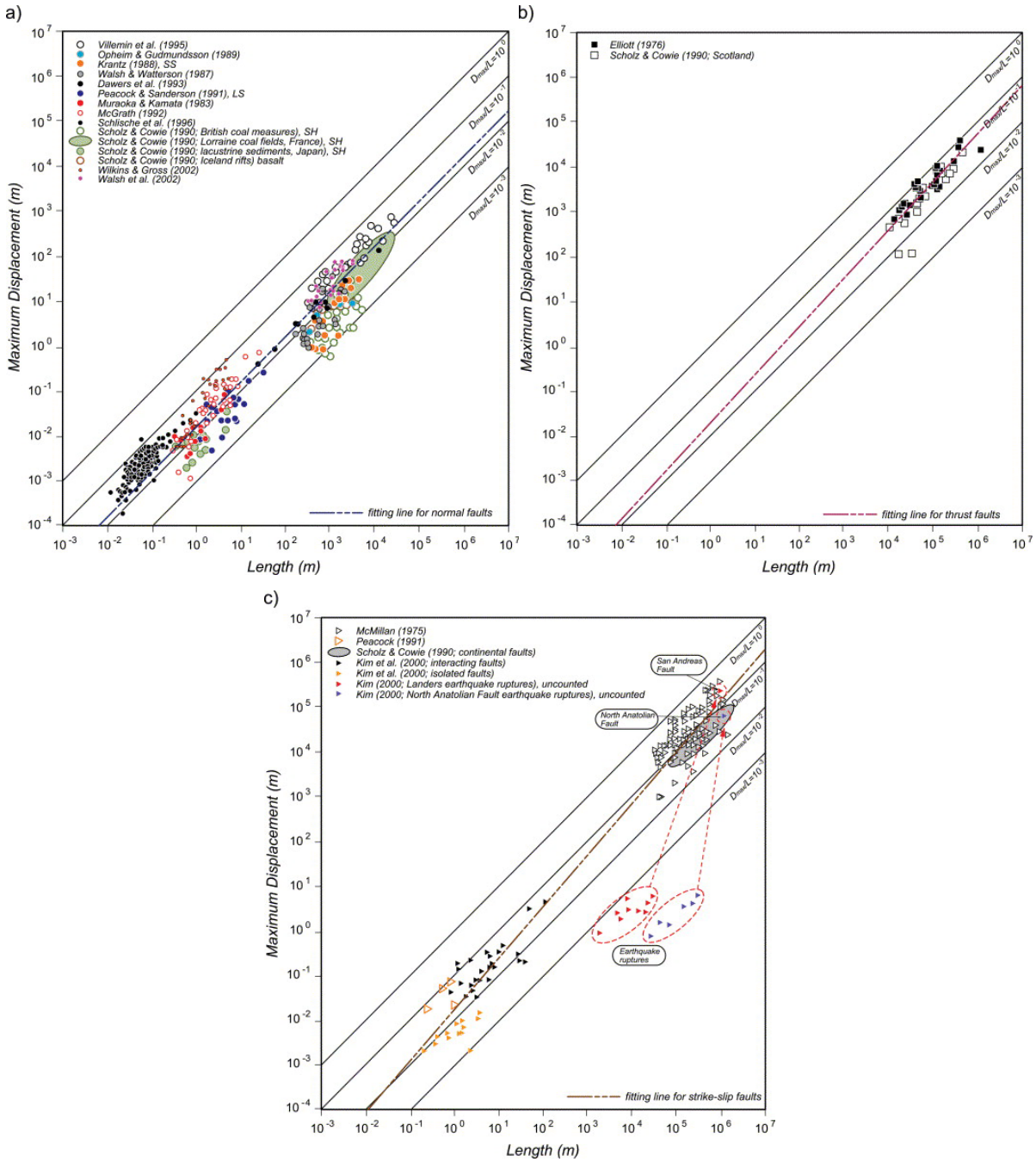

Figure 25 Correlation between fault length and fault displacement for normal faults (a), thrust faults (b) and strike-slip faults (c) from Kim & Sanderson (2005)

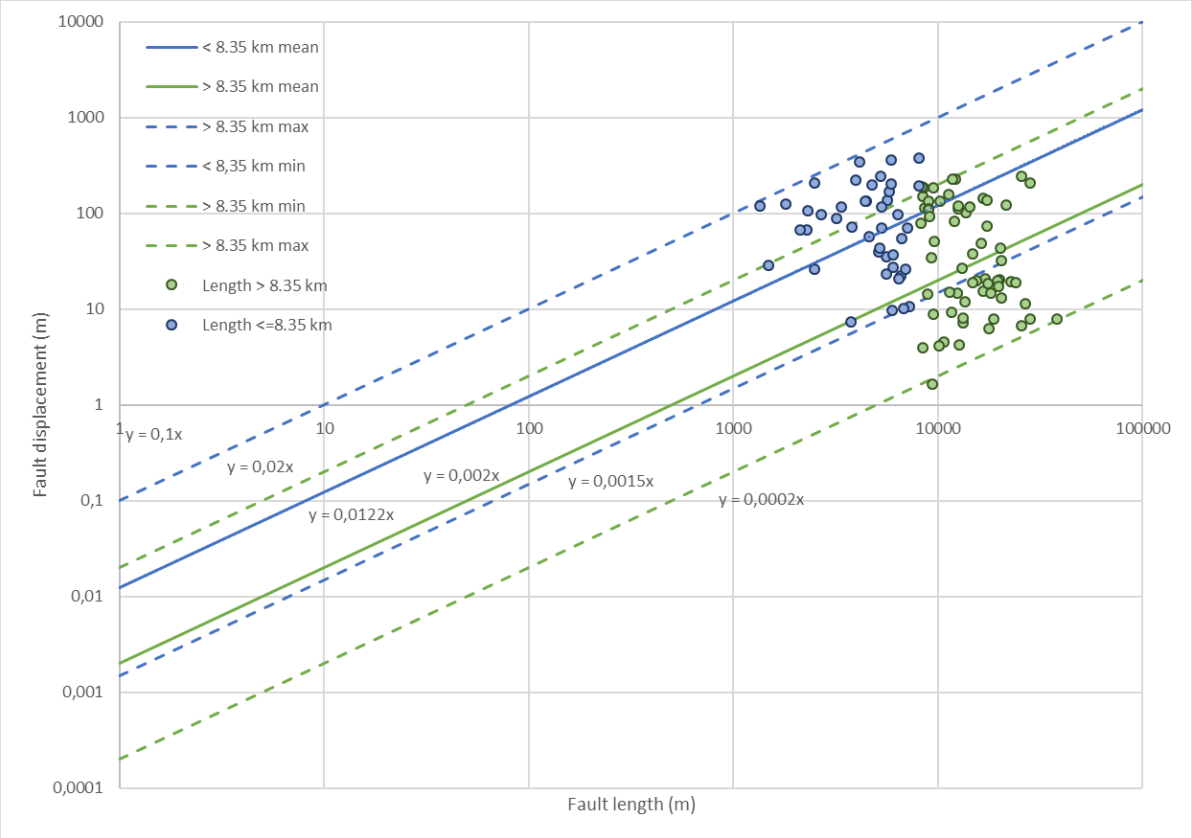

Figure 26 Correlation between fault length and fault displacement calibration using the data from the HIKE dataset from Belgium

In the data from the HIKE dataset it became evident, that longer normal faults had on average lower fault displacements than shorter faults. This is related to the simplification of the fault traces in the dataset, where fault zones with smaller faults have been simplified into one long single fault. Based on the available data a cut-off value of 8.35 km was selected to separate these two trends and apply different correlations for faults shorter than 8.35 km and faults longer than 8.35 km (Table 5).

Table 5 Correlations used for the different fault types for the calculation of the fault displacement from fault length

Fault type	Minimum	Average	Maximum
Normal fault < 8.35 km	y = 0.0015x	y = 0.0122x	y = 0.1x
Normal fault > 8.35 km	y = 0.0002x	y = 0.002x	y = 0.02x
Thrust fault	$y = 0.006x^{1.0796}$	$y = 0.02x^{1.0602}$	$y = 0.06x^{1.0796}$
Strike-slip fault	$y = 0.002x^{1.1398}$	$y = 0.017x^{1.1539}$	$y = 0.2x^{1.1398}$

3.5.2 Damage zone width

The damage zone width was calculated from the average fault displacement value based on the relationship for deformation bands (red lines in Figure 27) as published by Choi et al. (2015) (Figure 27, Table 6). Again minimum, average and maximum relationships were determined and calculated. To assess the impact of the chosen relationship on the extent of the damage zone, a comparison was done for average case using the Joint/Fracture relationship (blue lines in Figure 27). The difference is in the range of 3-50 m with a mean of 14 m.

Table 6 Correlations used for the calculation of the damage zone width from fault displacement (based on Choi et al. (2015))

Fault type	Minimum	Average	Maximum
All faults	$y = 0.05x^{0.6872}$	$y = 1.695x^{0.6872}$	$y = 35x^{0.6872}$

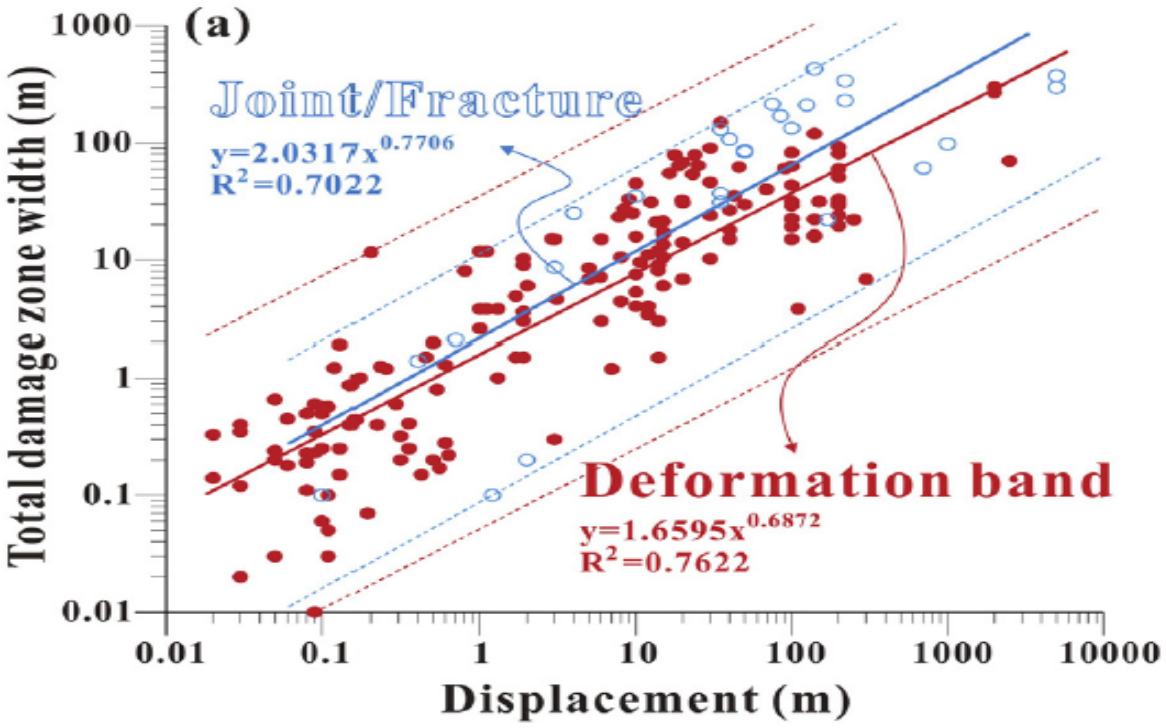

Figure 27 Correlation between damage zone width and fault displacement for the deformation band and the joint/fractures (Choi et al. (2015))

3.5.3 Fracture intensity

Mitchell & Faulkner (2012) published an equation that describes the relationship between fracture intensity, distance to the fault and width of the damage zone (Eq. 1). The same equation was also used by Reith (2018) for the calculation of the fracture intensity in the area of the California Geothermal doublet in the Netherlands.

$$F = e^{\frac{-X}{A}} \qquad \textit{eq. 1}$$

with:

F fracture intensity
X distance to fault
A width of the damage zone

This equation (Eq. 1) was solved to be used to calculate the distance from each fault for a selected list of fracture intensities (Eq. 2). In this case, the fracture intensity is normalized to a value of 1 at the location of the fault, the background fracture intensity of the rock is set to 0.2.

$$x = -ln(F)\,A \qquad \textit{eq. 2}$$

Figure 28 shows the distribution of fracture intensity with distance to the fault for 4 different example damage zones (1, 10, 100 and 1000 m).

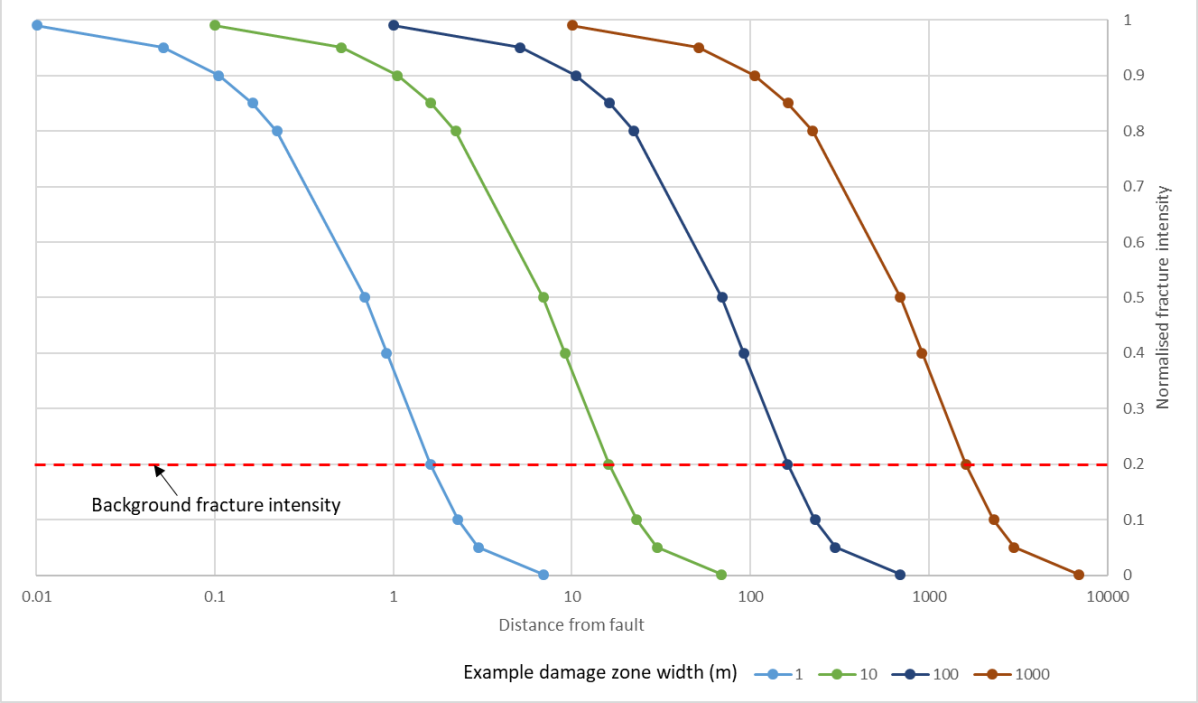

Figure 28 Fracture intensity as a relationship of damage zone width and distance from fault for 4 example damage zone widths. At a fracture intensity of 0.2 the fault no longer has an influence on the fracturing and is approximately equal to the maximum damage zone width.

Based on equation 2 three maps for the minimum, average and maximum case of the damage zone width (see figure 27) were calculated for 10 normalised fracture intensity iso-lines (0.001, 0.05, 0.1, 0.2, 0.5, 0.8, 0.85, 0.9, 0.95, 0.999). The minimum case was not included in the additional assessment, as the damage zone range was in a meter range for most faults and did not provide useful results for a regional assessment of permeability. Figure 29 shows the fracture intensity iso-lines for the average and maximum damage zone width cases.

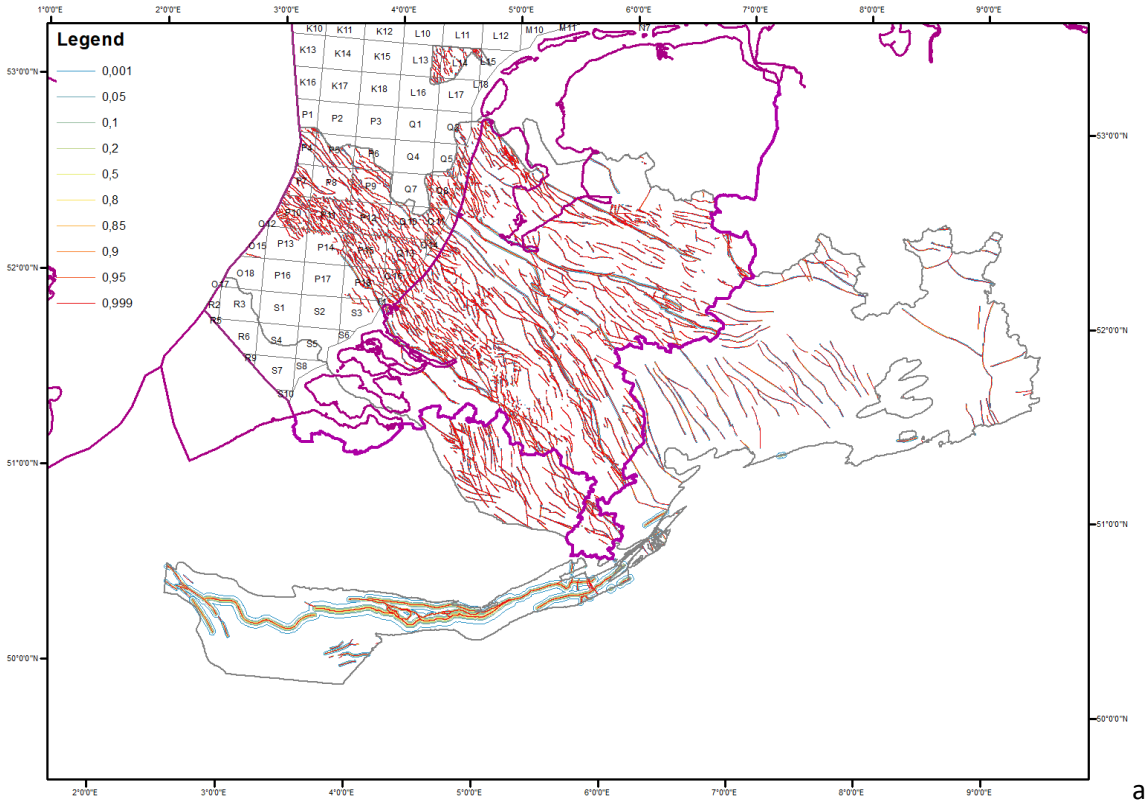

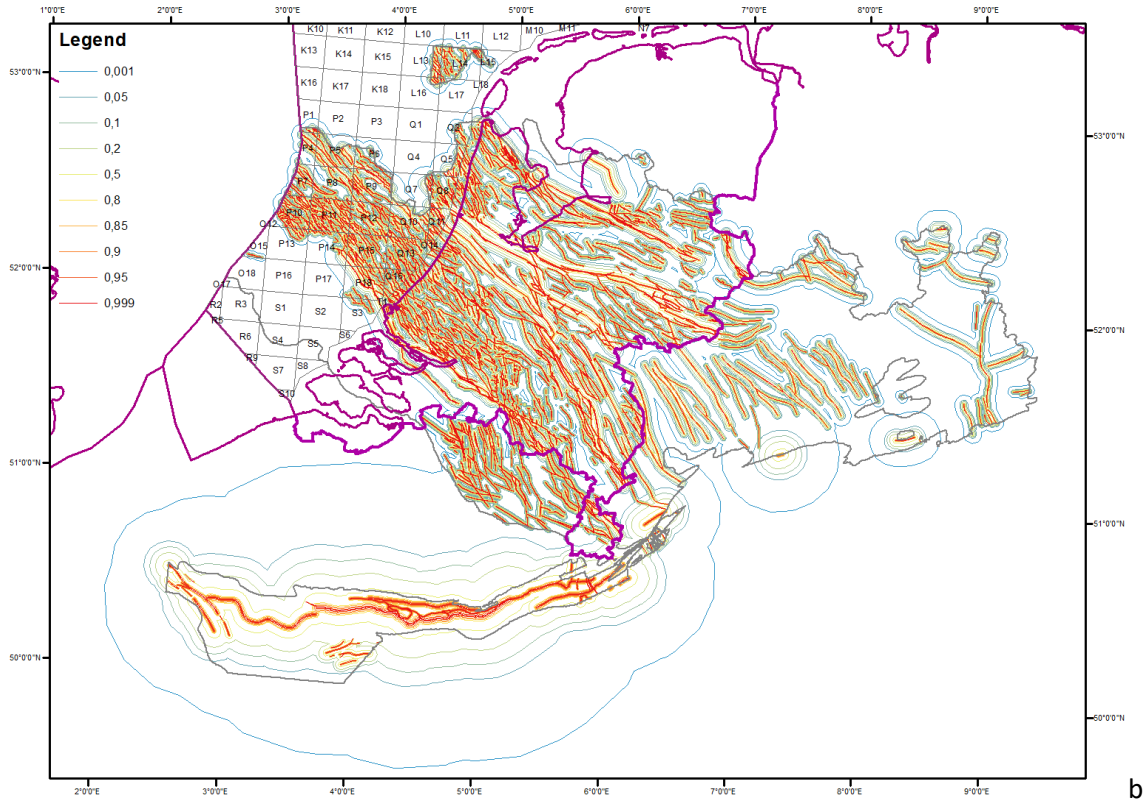

Figure 29 Fracture intensity iso-lines for the average damage zone width (a) and maximum damage zone width (b).

3.5.4 Fracture intensity to permeability

In order to calculate the permeability from the fracture intensity Mitchell & Faulkner (2012) defined the following equation, also applied by Reith (2018):

$$K = F^B \times C \qquad eq.\ 3$$

with:

K fracture permeability (mD)
B coefficient determined by trial and error (the permeability at boundary of damage zone must be equal the permeability value of the background fracture network) B = 2 (at fracture intensity of 0.2 equal to background permeability)
C permeability value at the fault core (mD)
F normalised fracture intensity.

The permeability at the fault core is the most uncertain factor in this equation. Several studies have published a wide variety of analyses, but due to the limitations of direct measurements in very heterogeneous environments these measurements vary by several factors (e.g., Caine et al. (1996); Michie et al. (2021) and references therein). In addition the fault core permeability is affected by several other parameters like the depth, direction of the fault with respect to the stress field, recent seismic activity or rock type (e.g. Caine et al. (1996)).

Transmissivity (product of permeability and net reservoir thickness) and flow model analyses for available geothermal installations and projects were used for calibration of the range of fault core permeabilities (Balmatt, pers. Comm.).

3.5.4.1 Fault core permeability calibration

In order to calculate the influence of present-day depth on the fault core permeability, the trend published by Michie et al. (2021) was used but adapted to the permeability values reported for e.g. the Balmat area. Based on the available permeability data, three trends were again defined for a minimum, average and maximum fault core permeability (Figure 30). In addition, the minimum depth for the faults was set to 500 m to avoid very high (unrealistic) permeabilities in shallower locations.

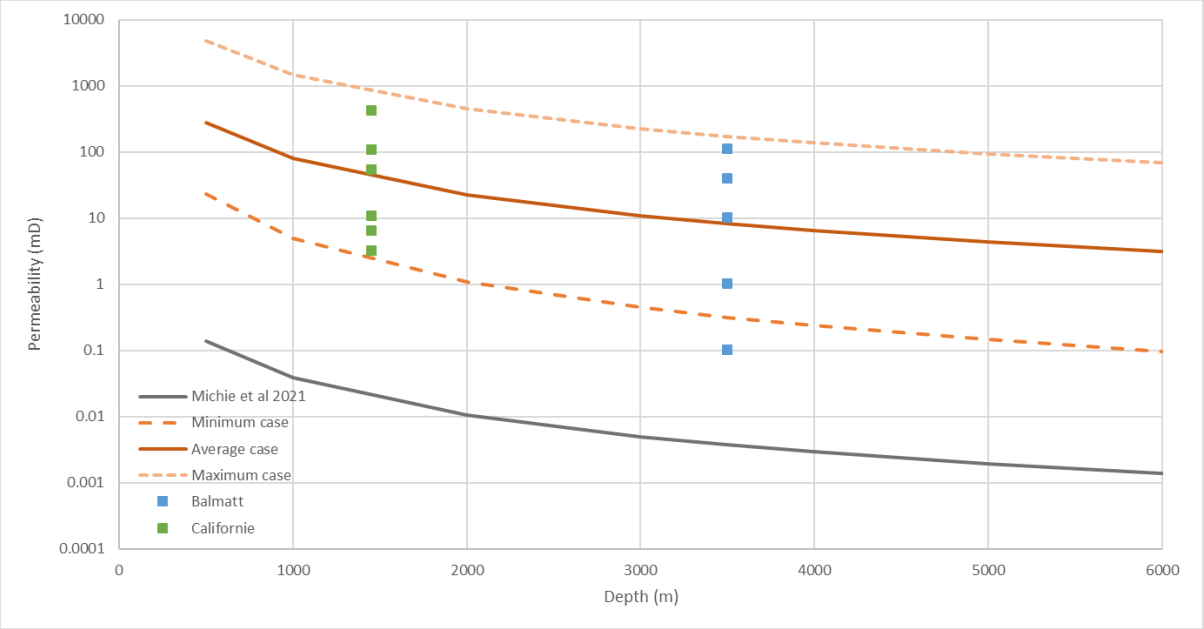

Figure 30 Modified permeability/depth trends used for the calibration of the fault core permeability. The grey line is the trend published by Michie et al. (2021), the orange lines are the trends for the maximum (dotted line), average (solid line) and minimum case (dashed line), the points are the calibration values from the Balmat and Californie aquifer models (personal comment and Reith, 2018)

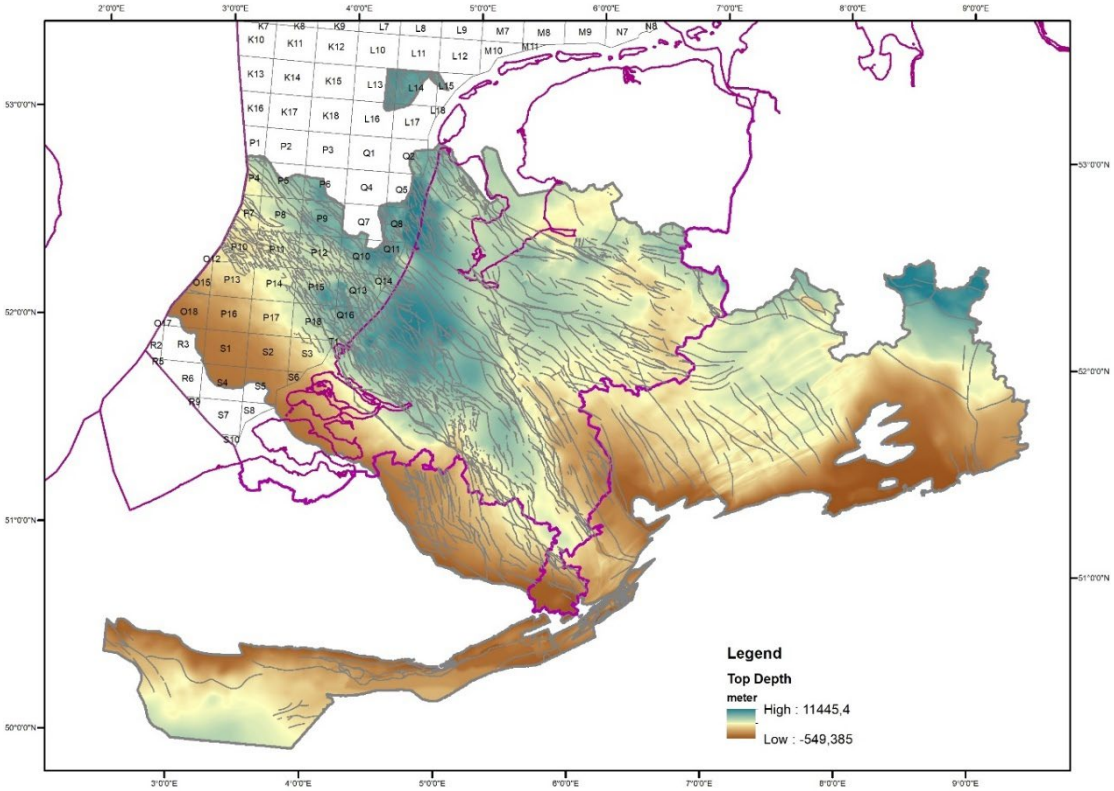

Figure 31 Present-day depth map with the location of the fault lines included in the permeability assessment.

The previously defined fracture intensity iso-lines were translated into points with a fixed distance of 500 m along the line and for each resulting point the present-day depth was gathered, based on the depth map, created in this project (Figure 31). For each point, the minimum, average and maximum

fault core permeability was then adjusted using the respective depth and trend as shown in Figure 30.

3.5.4.2 Fault direction

Another parameter influencing the fault core permeability is the direction of the fault. Several studies have shown that faults perpendicular to the maximum stress direction are more likely to the open for flow while faults parallel to the maximum stress are more likely to be closed. The average fault direction was included for all faults (with the exception of the French dataset). Based on the results of the SCAN UDG project (Osinga and Buik (2019) and the data from the World Stress Map (Heidbach et al. (2018), the direction of the maximum stress in the study area is approximately NNW-SSE. Based on this, all faults in the study area were given a permeability factor based on their relation with respect to the maximum stress (Figure 32). This factor was included in the calculation of the fault core permeability.

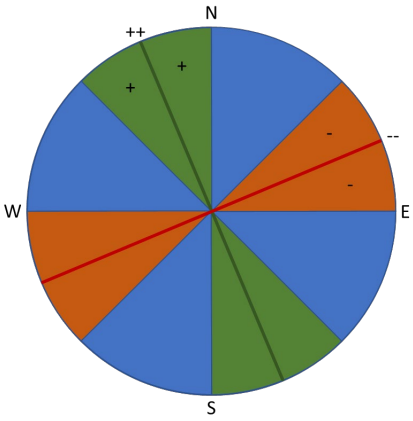

Figure 32 Illustration showing the relationship between fault direction and stress direction and assigned permeability factor: green – 1, blue – 0.1, red – 0.01

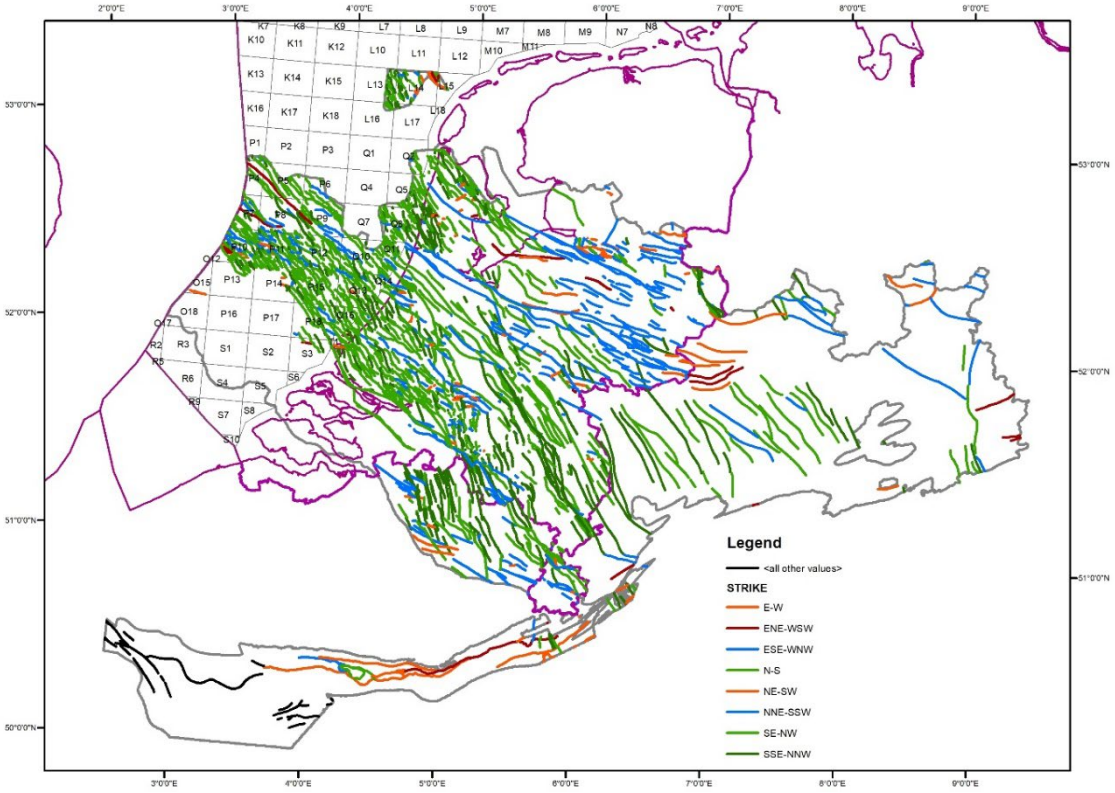

Figure 33 Map view showing the faults in the study area with the same colour coding for fault direction with respect to stress direction.

3.5.4.3 Recent fault activity

The third factor, that influences the fault core permeability is based on recent seismic activity. Faults that showed seismic activity recently are more likely to show a higher permeability compared to inactive faults. Based on the dataset of natural seismic activity from KNMI[1]all points within a 5 km radius around a measured seismic event were given a factor of 10 to highlight the higher probability for higher permeabilities. Figure 34 shows faults within the dataset that are within this 5 km radius.

[1] KNMI Earthquake catalogue, https://www.knmi.nl/kennis-en-datacentrum/dataset/aardbevingscatalogus, accessed Jan. 2022

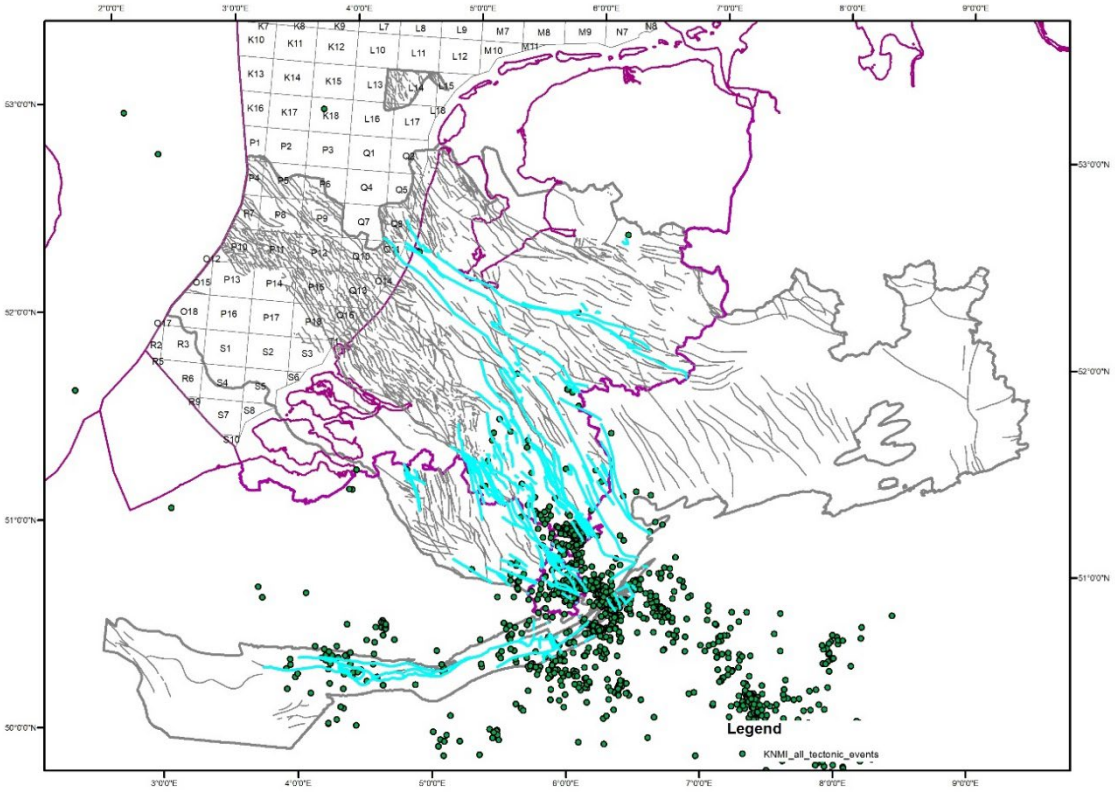

Figure 34 KNMI dataset of natural seismic activity (https://www.knmi.nl/kennis-en-datacentrum/dataset/aardbevingscatalogus) and highligted faults that are within a 5 km radius around these seismic events.

The final permeability calculation uses equation 3 and the adjusted fault core permeability (depth corrected and using the factors for fault direction and recent seismic activity) together with the fracturing intensity (F) for each point. Permeabilities lower than the defined matrix permeability were set to the value of the matrix permeability (see Table 3).

3.5.5 Other parameters – currently not considered in the calculation

3.5.5.1 Fault dip and presence

The current approach has a large uncertainty with respect to fault position and fault presence due to fault trace selection at the level of the Permian/top Carboniferous and no actual mapping of faults for the Dinantian. One possibility to account for the lateral uncertainty of the fault core in the Dinantian was to include a parameter that uses the fault steepness, where vertical or steep faults have a lower uncertainty while intermediate and gentle faults have a higher uncertainty. However, this approach does not include the actual uncertainty of the fault presence and was therefore omitted from the approach.

3.6 Permeability maps

The final maps combine the fracture permeability maps and the matrix permeability maps using IDW interpolation between the points. Ten maps are presented here, showing different minimum, average and maximum values for the fault core permeability and average and maximum values for the damage zone width combined with maps capturing the increased matrix permeability in the areas potentially affected by karstification.

It has to be noted that due to the overall large uncertainty with respect to the used assumptions and relationships as well as to the exact location and even presence of the faults in the Dinantian, these maps have to be considered are purely highlighting areas of interest for geothermal exploration and cannot be directly used as input for geothermal potential calculations for specific sites.

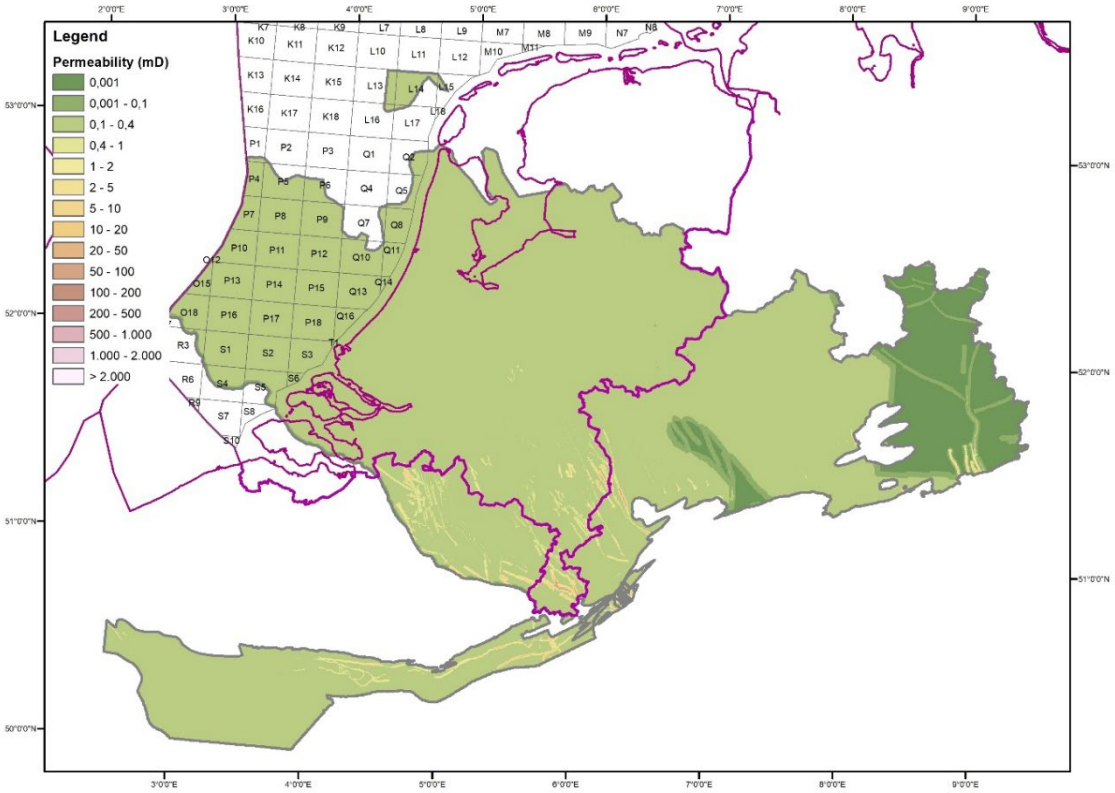

Figure 35 Permeability map using the average damage zone width and minimum fault core permeability cases, as well as the minimum matrix permeability.

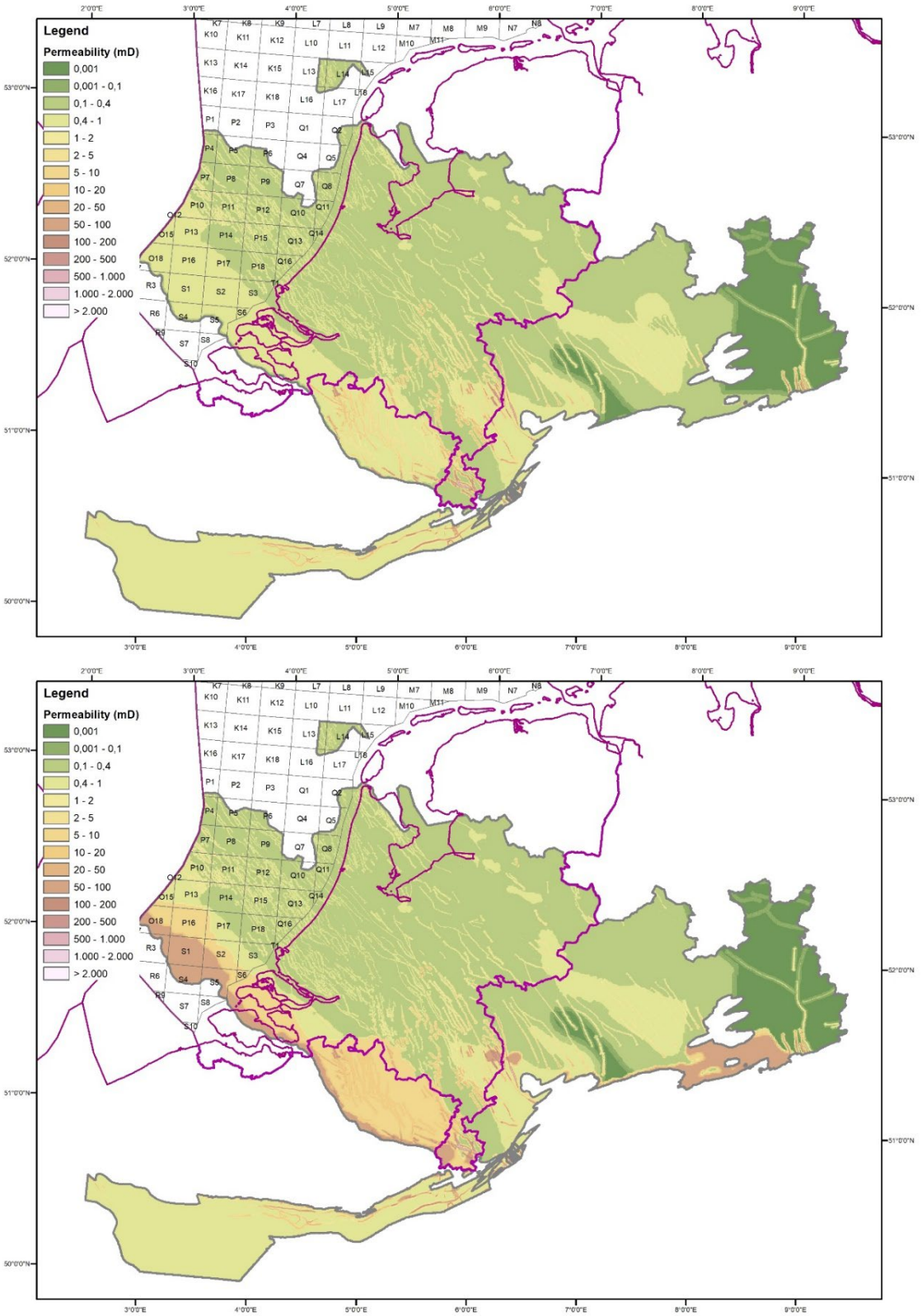

Figure 36 Permeability map using the average damage zone width and average fault core permeability cases, as well as the average matrix permeability, (a) without karst, (b) with potential karst.

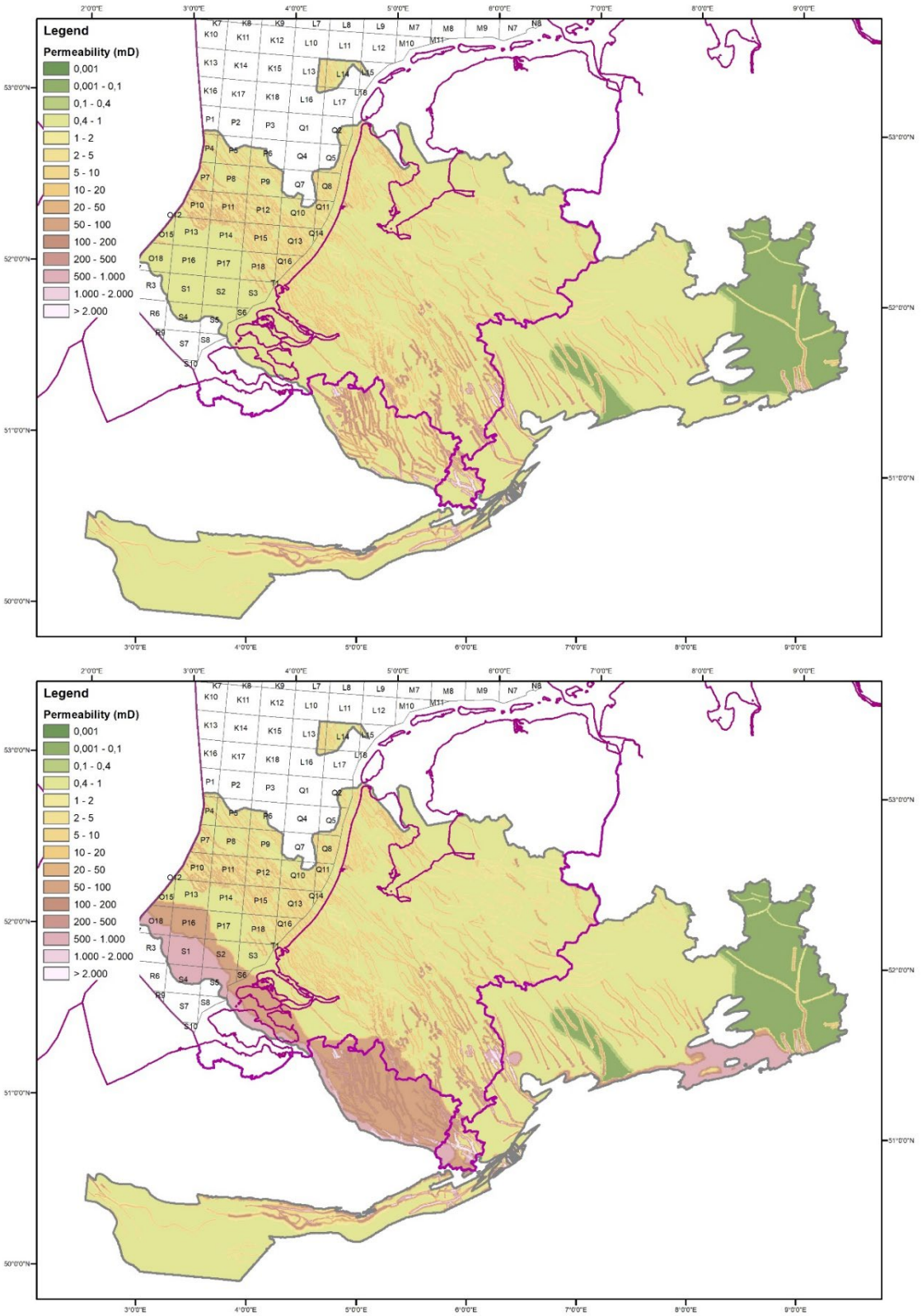

Figure 37 Permeability map using the average damage zone width and maximum fault core permeability cases, as well as the maximum matrix permeability, (a) without karst, (b) with potential karst.

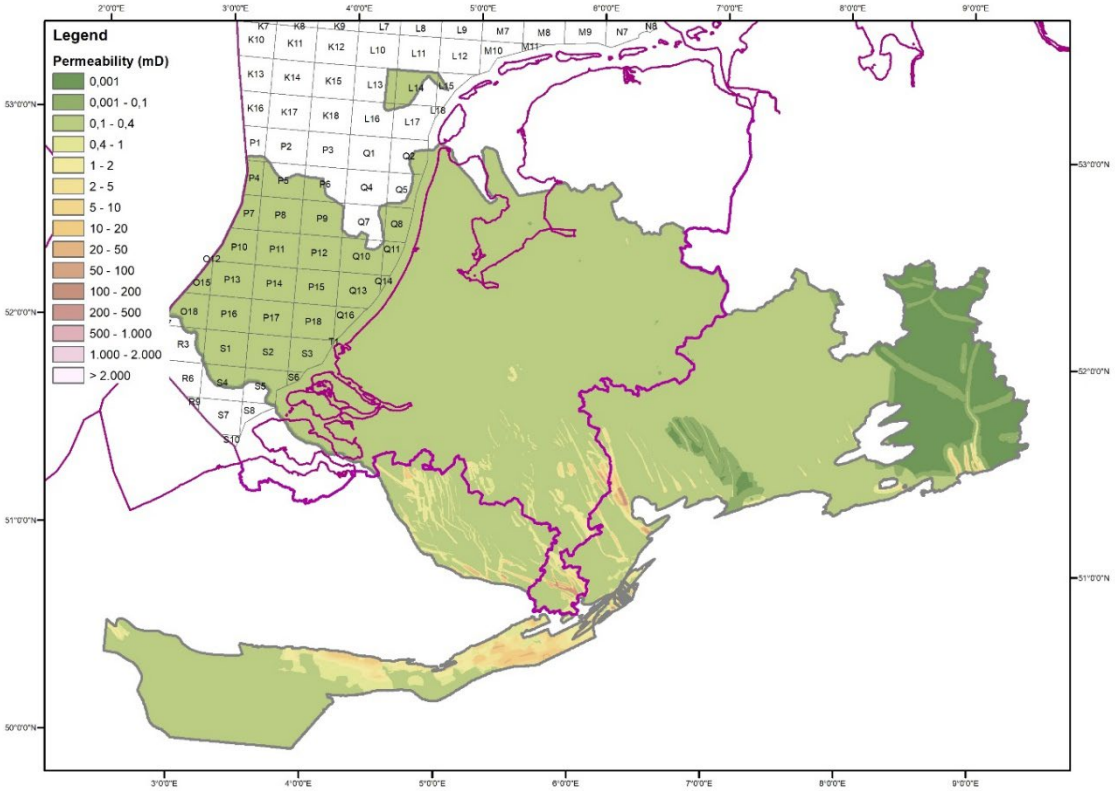

Figure 38 Permeability map using the maximum damage zone width and minimum fault core permeability cases, as well as the minimum matrix permeability.

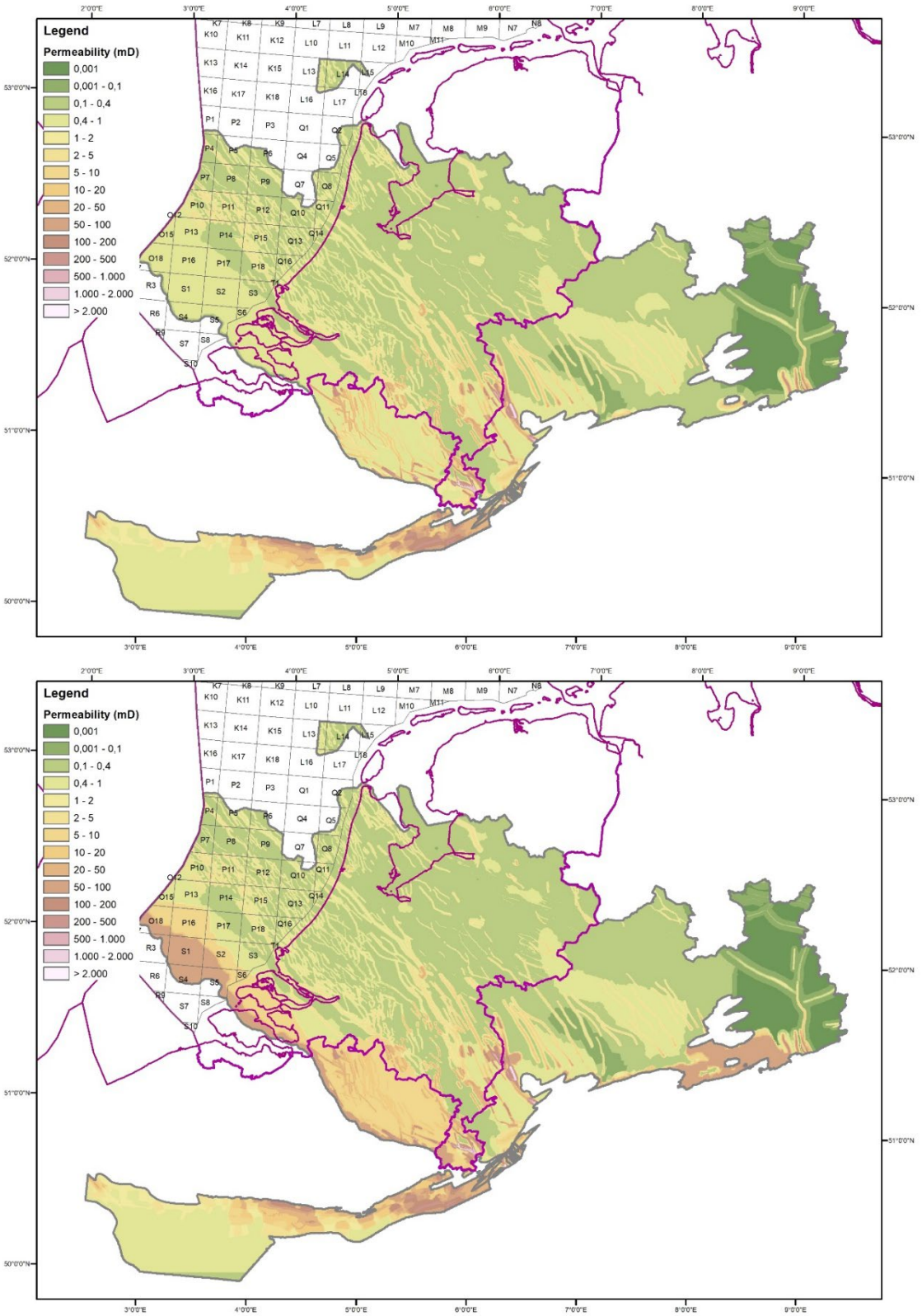

Figure 39 Permeability map using the maximum damage zone width and average fault core permeability cases, as well as the average matrix permeability, (a) without karst, (b) with potential karst.

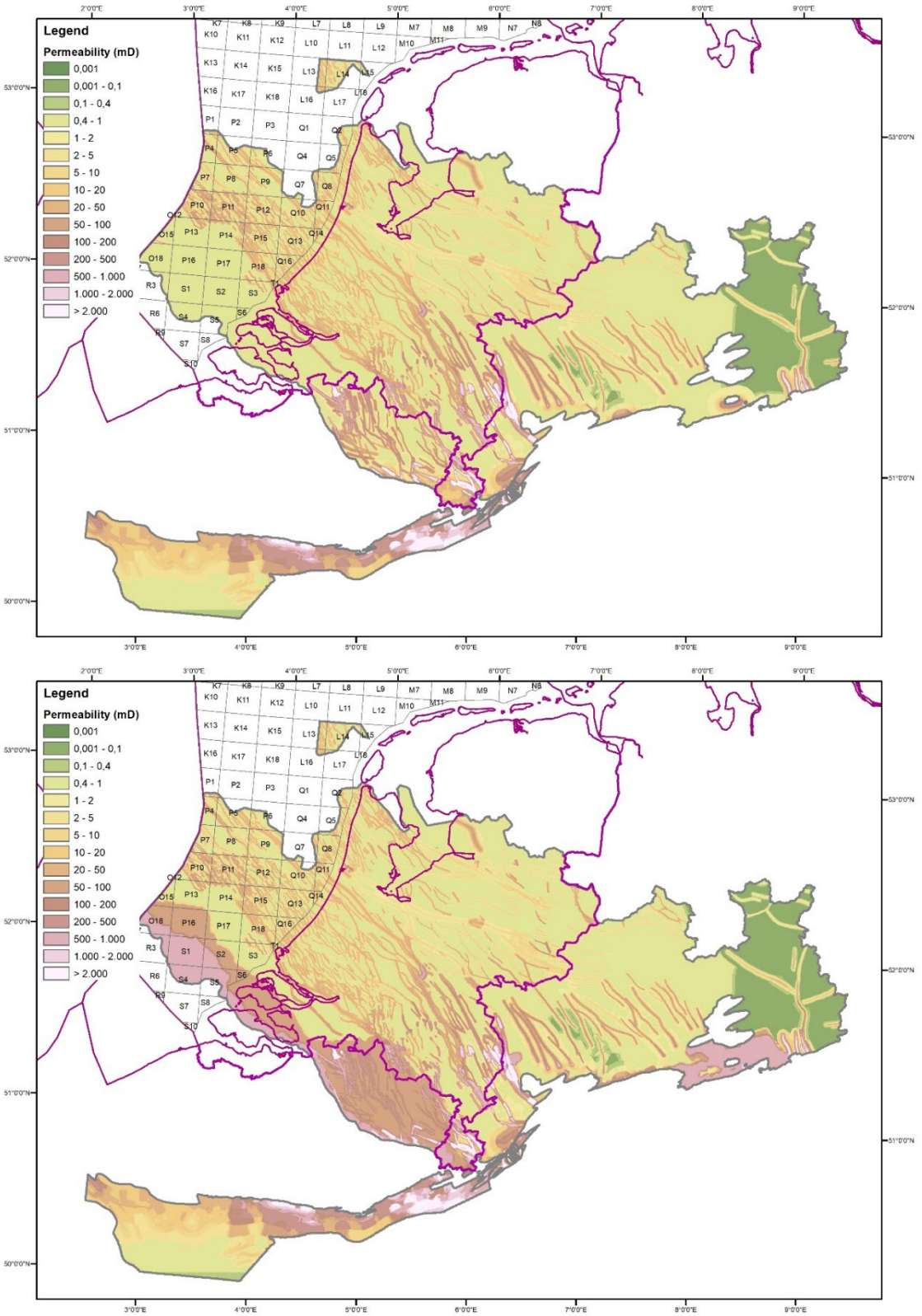

Figure 40 Permeability map using the maximum damage zone width and maximum fault core permeability cases, as well as the maximum matrix permeability, (a) without karst, (b) with potential karst.

4 Geothermal potential

4.1 Heat in Place (HIP)

The volumetric 'Heat in Place' (HIP) method, developed by the United States Geological survey (USGS) and reported by Muffler & Cataldi (1978), with subsequent revisions and reformulations (Garg & Combs (2010); Garg & Combs (2011); Garg & Combs (2015); Williams et al. (2008)), is the most globally used evaluation technique to estimate the available heat from deep geothermal aquifers among geological services, research centres and companies in general. A HIP estimation is the first and the key step of any geothermal project in early exploration stages. This method calculates the heat in energy per unit area, which is present in a geothermal aquifer, with respect to an arbitrary cooling temperature which is usually set to surface or ambient temperature. The method requires estimates on aquifer depth and thickness, temperature, and the aquifer rock properties heat capacity, density, porosity, and water specific heat and density. The HIP is the maximum theoretically extractable heat energy in the aquifer and is defined by:

$$HIP = \left[(1-\varphi)c_{pr}\rho_r + \varphi C_{pw}\rho_w\right] \times h \times \left(T_r - T_{ref}\right) \qquad \textit{eq. 4}$$

Table 7 lists the parameters and the common parameter values that were adopted from the HOTLIME project. The temperature map described in chapter 2 was used as aquifer temperature. The HIP is calculated as energy per unit area. Figure 41 shows the resulting heat in place. Note that, unlike over the London Brabant Massif in Belgium where the aquifer does not occur, the large grey areas in the Netherlands are not related to its absence. The quality of the data in this area is however such that it was not possible to determine the thickness of the aquifer. Also note that, although several areas with HIP around ~500 GJ/m² attract attention as having the highest *heat content*, these are not necessarily the most attractive areas for geothermal *production* – heat content alone does not say anything about the possibility that the subsurface energy can in fact be produced. The conversion from HIP to geothermal resources involves an estimate of the recoverability of the heat using extraction techniques when defining technical resources (Figure 1 PRH) or, when dealing with economic resources, the project economy (Figure 1 RH). In the next section the potential of the productivity of the Dinantian limestone will be assessed.

Table 7 Rock thermal properties used for the heat in place calculation.

	description	unit	value
Q_{total}	energy content for a column of aquifer rock	J / m²	
ϕ	bulk porosity	fraction	0.05
c_{pr}	heat capacity of the aquifer rock (matrix)	J / kg.K	1000
c_{pw}	heat capacity of the pore fluid (brine)	J/ kg.K	3800
ρ_r	rock matrix density of the aquifer rock	kg/m³	2700
ρ_w	density of low TDS water at about 100°C	kg/m³	1040
h	net aquifer height	m	-
T_r	aquifer temperature	°C	-
T_{ref}	reference (injection) temperature	°C	10

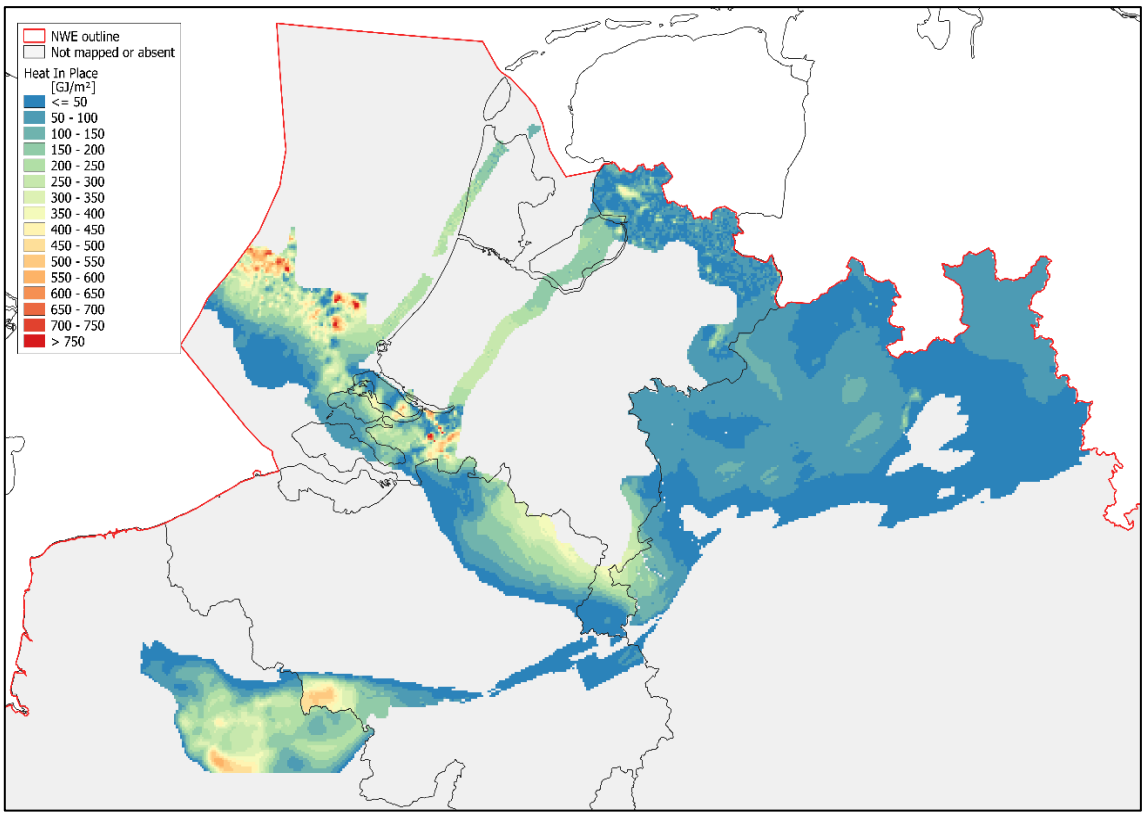

Figure 41 Heat in Place.

4.2 Potential power

In contrast to the heat in place method, the ThermoGIS method (Vrijlandt et al. (2020)) considers the assumed flow properties. Following Van Wees et al. (2012), the geothermal power that can be extracted by a heat exchanger is:

$$P_{he} = Q_m \times dT \times c_p \qquad \textit{eq. 5}$$

with:

P_{he}	geothermal power [W_{th}]
Q_m	mass flow rate [g/s]
dT	difference between the production and injection temperatures of the brine [°K]
c_p	brine heat capacity [J/g°K]

The return temperature was set to 30 °C for the current study. The above-mentioned flow rate depends on the applied pressure, the doublet configuration and the subsurface properties as follows:

$$Q_v = \Delta P \frac{2\pi kH}{\mu\left(ln\left(\frac{L}{r_w}\right)+S\right)} \qquad \textit{eq. 6}$$

with:

Q_v	volume flow rate [m^3/s] (*convert to/from mass flow rate Q_m using the brine density*)
ΔP	pressure difference at the well – aquifer interface [Pa]
k	permeability [m^2] (*1 -more commonly used- Darcy equals 9.869233e-13 m^2*).
H	net aquifer height [m]

μ brine viscosity [Pa.s]
L distance between producer and injector wells at aquifer level [m]
r_w radius of the well [m]
S skin factor [-]

Hence, the key subsurface variables that determine the geothermal power are the net thickness of the aquifer and the permeability. The variability of the brine viscosity is evidenced to be far less important than the variability of thickness and permeability. ThermoGIS and its calculation engine DoubletCalc determine the flow rate by assuming a standard well radius of 8.5“ for the current study. It performs a two-step optimization. The well distance between the producer and injector wells at aquifer level is optimized first, followed by the imposed pressure difference between well and aquifer. A large well distance at aquifer level between producer and injector increases the required pump pressure, while a small distance accelerates the thermal breakthrough. The maximum allowed cooling of the production water after 50 years was set to 10% of the difference between the initial aquifer temperature and the return temperature for the current study. The well distance is then minimized, while at the same time the 10% maximum cooling within the 50-year period is not exceeded. Next, the pump pressure is optimized. Theoretically, a higher pump pressure results in a higher flow rate and therefore a higher geothermal power. On the other hand, a higher pump pressure increases the costs of operating the pump and possibly results in a higher cost per unit energy. Furthermore, the pump pressure is limited by the pump specifications (set to 300 bar for the current study) and concerns of the integrity of the aquifer and the sealing capacity of the aquitard (very high pressures may damage the aquifer; currently, guidelines of the Dutch State Supervision on the Mines are used). Within these constraints, the pump pressure is optimized towards a minimum cost per unit energy. The latter is calculated using a discounted cashflow model based on data available for Dutch geothermal systems (Vrijlandt et al. (2020)). Because of the dependency on permeability, and the uncertainty therein, ThermoGIS requires the availability of a permeability uncertainty map, which is used to calculate geothermal power probability maps in terms of the P90[2], P10 etc.. Among the standard outputs of ThermoGIS are the achievable flow rate and the potential power, and various other maps like coefficient of performance (COP), unit technical cost (UTC) a.o.

ThermoGIS was developed for use with siliciclastic rocks from aeolian, marine and fluvial origin. Rock properties like porosity and permeability in these kinds of rocks are considered be spatially correlated over relatively large distances – a measurement of a property at a certain location can be used to predict this property at a location that is 100s to 1000s of meters away. If measurements of the property were made at a sufficient number of locations, an estimate of the property can be made at any unsampled location by interpolation. Limestone aquifers such as the Dinantian that rely on fracture and karst permeability do not meet this criterium. If a well is drilled in a high permeability fault or karst zone, the permeability in the nearby undamaged Dinantian aquifer rock is probably still very low. For a reliable flow prediction a detailed aquifer model is required. However, if a transmissivity map is constructed which represents the likely average aquifer permeability (representing a weighted average of the part of the aquifer that is considered to contribute to the doublet flow), sensible flow rates and geothermal power estimates can be calculated. This concept

[2] The P90 geothermal power is the minimum pre-drill determined geothermal power that will be achieved with 90% certainty, given the uncertainties of the input parameters.

was applied with acceptable results to one of the Californië doublets in Grubbenvorst (NL) (Veldkamp (2013)).

As was explained in chapter 3, assessing the fault and karst permeability is difficult, due to the spatial variability and the lack of measured permeability data. Therefore, the ten permeability scenario maps that were calculated (see Table 8) were all used individually for a ThermoGIS calculation. Rather than making use of a permeability standard error map, a standard error of 0.0001 was assumed. This means that uncertainty maps (P90, P10, etc.) cannot be calculated. Instead, the variation between the 10 resulting geothermal power maps is an indication of the uncertainty of the permeability maps. Figure 42 shows the resulting ten potential power maps, which must be considered 'equally likely'.

Areas with karst potential (scenarios 3, 5, 8, 10) can be differentiated from areas with fault potential (4, 5, 9, 10)– the locations of the HIKE-database faults clearly show in the potential power maps.

Rather than focusing on local high potential areas, for which the maps cannot be used, the complete set of maps may serve as an indicator or larger areas that may be prospective. Areas shaded in grey (not mapped) should be ruled out from any judgement regarding their geothermal potential – usually the data availability for those areas is too low for even an assessment of depth and/or thickness, leave alone potential.

Areas that show up in shades of red on most maps are areas with the highest possible potential.

Table 8 Permeability scenario descriptions. Shading refers to possible potential: light green = unfavourable, dark green = favourable.

scenario	damage zone width	fault core permeability	matrix permeability	karst	map
1	average	minimum	minimum	no	Figure 35
2	average	average	average	no	Figure 36a
3	average	average	average	yes	Figure 36b
4	average	maximum	maximum	no	Figure 37a
5	average	maximum	maximum	yes	Figure 37b
6	maximum	minimum	minimum	no	Figure 38
7	maximum	average	average	no	Figure 39a
8	maximum	average	average	yes	Figure 39b
9	maximum	maximum	maximum	no	Figure 40a
10	maximum	maximum	maximum	yes	Figure 40b

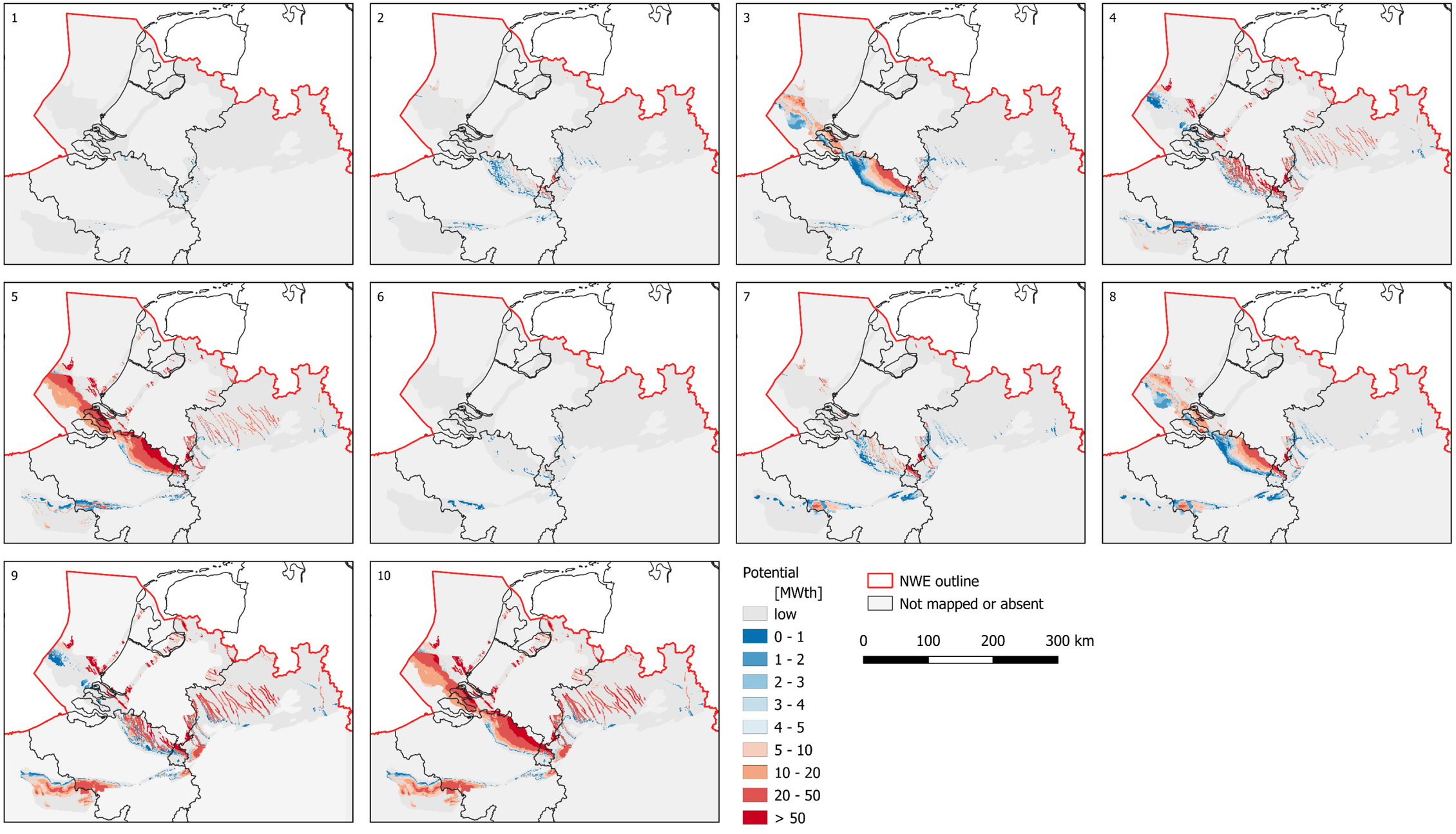

Figure 42 Potential power maps resulting from the 10 permeability scenarios.

5 Conclusions and recommendations

The goal of the research was to generate geothermal potential maps of the Dinantian. Due to a lack of measured aquifer quality data, and uncertainty regarding the geological factors that determine permeability, the calculated maps are indicative. The main achievement of the calculations is that areas of possible potential can be delineated on the maps.

5.1 Temperature

A very heterogeneous set of national temperature data was used to construct a temperature map at the level of the Dinantian. The dataset consists of bottom hole temperatures, well temperature gradients, maps based on a constant gradient, 3D model of Kriged temperature, and a steady state temperature model combined with a data assimilation procedure.

The accuracy of the temperature map largely depends on the available temperature data. When 3D modelled temperatures are combined with 2D constant gradient maps, border effects are expected. This is especially the case between Flanders and the Netherlands, and North Rhine-Westphalia and the Netherlands. In the latter case, the depths of the Top Dinantian along both sides of the border has not yet been fully harmonized, which enhances the existence of a temperature break.

The resulting temperature map could be improved if all data are brought together in a single modelling tool, in which a full temperature map is generated, rather than the patching of existing country maps and scattered well data.

Cross-checking the calculated Top Dinantian temperature map with measured production water temperatures from two deep geothermal wells in the Netherlands (CAL-GT-01) and Flanders (MOL-GT-01) suggest that predicted temperatures are in good agreement with the measured well data. Although the map was generated using assumptions that differ by country, the regional trends in temperature distribution are captured well.

5.2 Permeability

Measured permeability data are scarce and the spatial continuity of the permeability is inherently low. Therefore the compilation of a 2D permeability map of the Dinantian requires that permeability *concepts* are adopted and embedded in the workflow. Literature information about the correlation of fault displacement, fault damage zone width and related permeabilities were combined with the sparse available information on measured permeabilities, and geological concepts about karst occurrence which is primarily bedding parallel. Because these scenario concepts are all uncertain, various scenarios with low, medium and high permeabilities were used to generate a set of 10 equally probable permeability maps that are considered to cover the entire range of ‘true’ permeabilities of the Dinantian in the area.

The set of maps could be improved if a Monte-Carlo approach was used for the calculation. This would require distribution functions of the uncertain properties. The results would include P10, P50, P90 maps per scenario.

Given the importance of the faults for the creation of the permeability maps, more emphasis should be laid on fault mapping on the actual level of the Dinantian, which stresses the need for seismic data that image the Dinantian at deeper levels of several kilometers.

Calibration of the resulting maps would benefit from the availability of more measured permeability data like well test results and fault permeabilities.

5.3 Geothermal potential

The generated heat in place map shows areas where the Dinantian aquifer has a high heat content and, as such, delineates the first-order potential areas. The heat in place method is robust and widely applied but does not give information about actual geothermal potential because it does not use flow property information (well productivity and injectivity).

Geothermal potential maps were calculated for the Dinantian using the ThermoGIS calculation tool. The set of 10 equally probable maps should be considered indicative, given the uncertainty in the input permeability maps.

For the set of assumptions used to generate the permeability maps, the highest potential areas are those where Cretaceous karstification has taken place or is considered to have occurred.

The maps are meant to highlight the higher-potential areas on a supra-regional scale and should by no means be used at a local scale.

Acknowledgements

Harmen Mijnlieff is thanked for fruitful discussions and careful review of the manuscript.

6 References

Agemar, T., Schellschmidt, R., & Schulz, R. (2012). Subsurface temperature distribution in Germany. Geothermics, *44*, 65-77. doi:https://doi.org/10.1016/j.geothermics.2012.07.002

Békési, E., Struijk, M., Bonté, D., Veldkamp, J. G., Limberger, J., Fokker, P. A., . . . Wees, J. D. v. (2020). An updated geothermal model of the Dutch subsurface based on inversion of temperature data. Geothermics, *88*, 1-17. doi:https://doi.org/10.1016/j.geothermics.2020.101880

Bense, V. F., Gleeson, T., Loveless, S. E., Bour, O., & Scibek, J. (2013). Fault zone hydrogeology. Earth-Science Reviews, *127*, 171-192. doi:https://doi.org/10.1016/j.earscirev.2013.09.008

Bonté, D., van Wees, J. D., Guillou-Frottier, L., Bouchot, V., & Serrano, O.Deep temperatures in the paris basin from tectonic-heat flow modelling. *European Geothermal Congress,* Pisa, Italy. 3-7 June, 2013

Bonté, D., Van Wees, J. D., & Verweij, H. (2012). Subsurface temperature of the onshore Netherlands: new temperature dataset and modelling. Netherlands Journal of Geosciences, *91*(4), 491-515.

Bruijnen, P. (2019). Estimating geothermal power of ultra-deep Dinantian carbonates in the Dutch subsurface. SCAN Utrecht.

Caine, J. S., Evans, J. P., & Forster, C. B. (1996). Fault zone architecture and permeability structure. Geology, *24*(11), 1025. doi:10.1130/0091-7613(1996)0242.3.CO;2

Carlson, T. (2019). Petrophysical report of the Dinantian carbonates in the Dutch subsurface. SCAN Utrecht.

Childs, C., Manzocchi, T., Walsh, J. J., Bonson, C. G., Nicol, A., & Schöpfer, M. P. J. (2009). A geometric model of fault zone and falt rock thickness variations. Journal of Structural Geology, *31*(2), 117-127. doi:https://doi.org/10.1016/j.jsg.2008.08.009

Choi, J. -., Yang, S. -., Han, S. -., & Kim, Y. -. (2015). Fault zone evolution during Cenozoic tectonic inversion in SE Korea. Journal of Asian Earth Sciences, *98*, 167-177. doi:http://dx.doi.org/10.1016/j.jseaes.2014.11.009

Garg, S. K., & Combs, J. (2010). Appropriate use of USGS volumetric “Heat in place” method and monte carlo calculations. SGP-TR-188. ***Thirty-Fourth Workshop on Geothermal Reservoir Engineering,*** Stanford University, Stanford, California.

Garg, S. K., & Combs, J. (2011). A re-examination of USGS volumetric “Heat in place” method. ***Thirty-Sixth Workshop on Geothermal Reservoir Engineering. SGP-TR-191.*** Stanford University, Stanford, California.

Garg, S. K., & Combs, J. (2015). A reformulation of the USGS volumetric 'heat in place" resource estimation method. Geothermics, *55*, 150-158. doi:http://dx.doi.org/10.1016/j.geothermics.2015.02.004

Gies, C., Struijk, M., Békési, E., Veldkamp, J. G., & Wees, J. D. v. (2021). An effective method for paleo-temperature correction of 3D thermal models: A demonstration based on high resolution datasets in the Netherlands. Global and Planetary Change, *199*, 1-15. doi:https://doi.org/10.1016/j.gloplacha.2021.103445

Heidbach, O., Rajabi, M., Cui, X., Fuchs, K., Müller, B., Reinecker, J., . . . Zoback, M. D. (2018). The World Stress Map database release 2016: Crustal stress pattern across scales. Tectonophysics, *744*, 484-498. doi:http://doi.org/10.1016/j.tecto.2018.07.007

Kim, Y., & Sanderson, D. J. (2005). The relationship between displacement and length of faults: a review. Earth-Science Reviews, *68*(3–4), 317-334. doi:http://dx.doi.org.proxy.library.uu.nl/10.1016/j.earscirev.2004.06.003

Kramers, L., Van Wees, J. D., Pluymaekers, M. P. D., Kronimus, A., & Boxem, T. (2012). Direct heat resource assessment and subsurface information systems for geothermal aquifers; the Dutch perspective. Netherlands Journal of Geosciences, *91*(04), 637-649.

Licour, L. (2012). *Relations entre la géologie profonde et le comportement hydrogéologique du réservoir géothermique du hainaut (belgique) - caractérisation de l'aquifère dans la région de saint-ghislain* (PhD thesis).

Michie, E. A. H., Kaminskaite, I., Cooke, A. P., Fisher, Q. J., Yielding, G., & Tobiss, S. D. (2021). Along-strike permeability variation in carbonate-hosted fault zones. Journal of Structural Geology, *142* doi:https://doi.org/10.1016/j.jsg.2020.104236

Mitchell, T. M., & Faulkner, D. R. (2012). Towards quantifying the matrix permeability of fault damage zones in low porosity rocks. Earth and Planetary Science Letters, *339–340*, 24-31. doi:http://dx.doi.org/10.1016/j.epsl.2012.05.014

Mozafari, M., Gutteridge, P., Riva, A., Geel, K., Garland, J., & Dewit, J. (2019). Facies analysis and diagenetic evolution of the Dinantian carbonates in the Dutch subsurface. SCAN Utrecht.

Muffler, L. J. P., & Cataldi, R. (1978). Methods for Regional Assessment of Geothermal Resources. Geothermics, *7*, 53-89.

Reith, D. F. H. (2018). *Dynamic simulation of a geothermal reservoir. case study of the dinantian carbonates in the californië geothermal wells, limburg, NL* (MSc Thesis).

Sun, S., & Pollitt, D. A. (2021). Optimising development and production of naturally fractured reservoirs using a large empirical dataset. Petroleum Geoscience, *27*(2) doi:https://doi.org/10.1144/petgeo2020-079

ten Veen (editor), J. H. (2021). Final fault data collection report and database. GeoERA HIKE deliverable D2.2b.

Van Leverink, D. J., & Geel, C. R. (2019). Fracture Characterization of the Dinantian Carbonates in the Dutch Subsurface. SCAN Utrecht.

Van Wees, J. D., Kronimus, A., Van Putten, M., Pluymaekers, M., Mijnlieff, H., Van Hooff, P., . . . Kramers, L. (2012). Geothermal aquifer performance assessment for direct heat production–Methodology and application to Rotliegend aquifers. Netherlands Journal of Geosciences, *91*(04), 651-665.

Vandenberghe, N., & Fock, W. (1989). Temperature data in the subsurface of Belgium. Tectonophysics, *164*(2-4), 237-250. doi:https://doi.org/10.1016/0040-1951(89)90017-6

Veldkamp, J. G. (2013). Advies aanvraag Garantieregeling AARD03001 CLG Californië (downloaded from https://data.rvo.nl). TNO Utrecht.

Veldkamp, J. G., Großmann, J., de Witt, A., Rupf, I., Porpaczy, C., Franců, J., . . . Ogna, M. (2021). Report on play and prospect evaluation. GeoERA HotLime deliverable 3.1.

Veldkamp, J. G., & Hegen, D. (2020). Temperature modelling of the Dutch subsurface at the depth of the Dinantian (downloadable from https://nlog.nl/en/scan). SCAN Utrecht.

VITO, TNO, & Grontmij. (2014). GEOHEAT-APP: Economische haalbaarheid van intermediaire en diepe geothermie voor het verduurzamen van de warmtevraag bij bouw- en renovatieprojecten. VITO, TNO report projectbrochure, Mol (B), Utrecht (NL).

Vrijlandt, M. A. W., Struijk, E. L. M., Brunner, L. G., Veldkamp, J. G., Witmans, N., Maljers, D., & Van Wees, J. D. (2020). ThermoGIS: From a static to a dynamic approach for national geothermal resource information and development. *Proceedings World Geothermal Congress,* Reykjavik, Iceland. 26 April - 2 May 2020

Williams, C. F., Reed, M. J., & Mariner, R. H. (2008). **A review of methods applied by the U.S. Geological Survey in the assessment of identified geothermal resources**. United States Geological Survey report U.S. Geological Survey Open-File Report 2008-1296,

Appendix A: Borehole temperature data

Borehole temperature data for Wallonia, based on SGB data. Borehole temperatures (blue circles) are plotted agaiwnst depth. Orange line represents linear temperature gradient calculated based on the borehole temperature data for a 10°C surface temperature. Borehole coordinates are provided in Section 2.2.4.

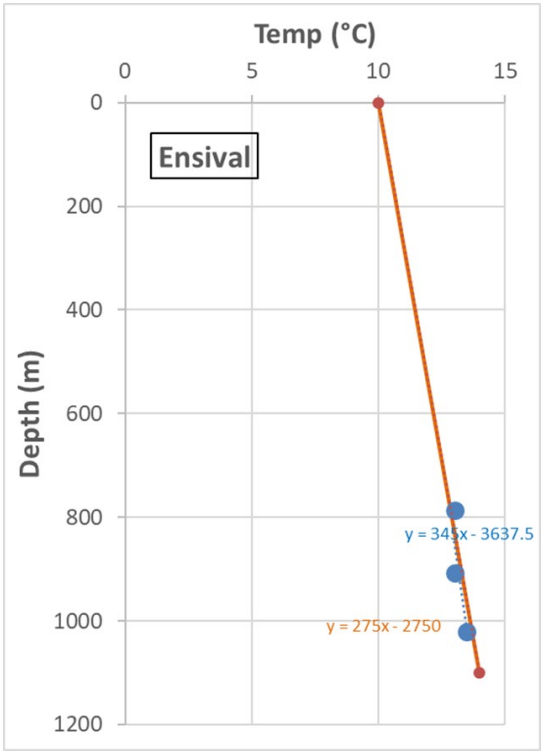

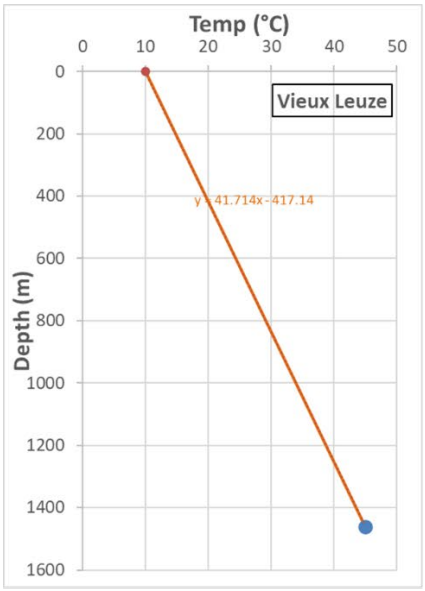
Temp (°C)
Vieux Leuze
y = 41.714x - 417.14
Depth (m)

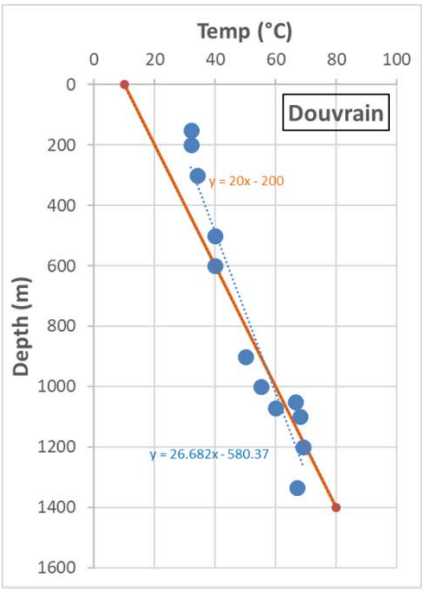
Temp (°C)
Douvrain
y = 20x - 200
y = 26.682x - 580.37
Depth (m)

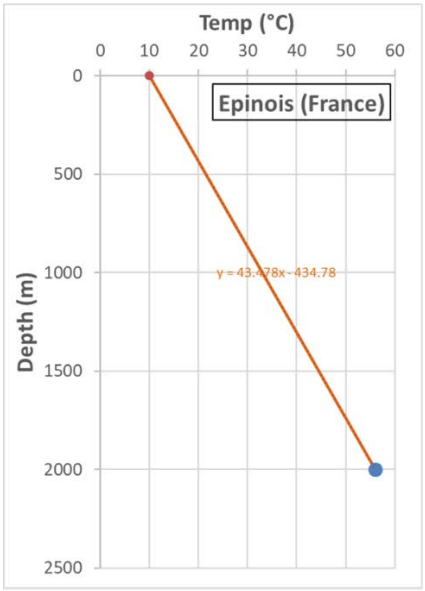
Temp (°C)
Epinois (France)
y = 43.478x - 434.78
Depth (m)

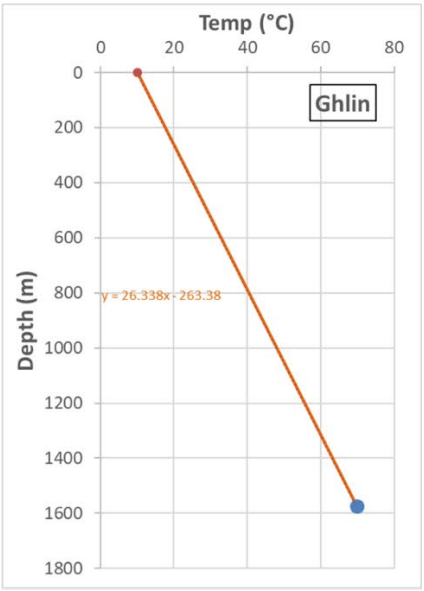
Temp (°C)
Ghlin
y = 26.338x - 263.38
Depth (m)

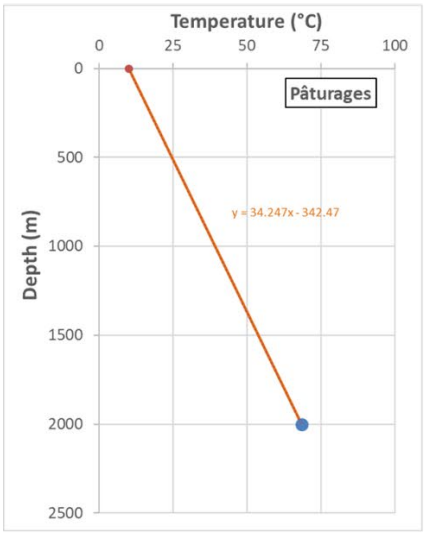
Temperature (°C)
Pâturages
y = 34.247x - 342.47
Depth (m)

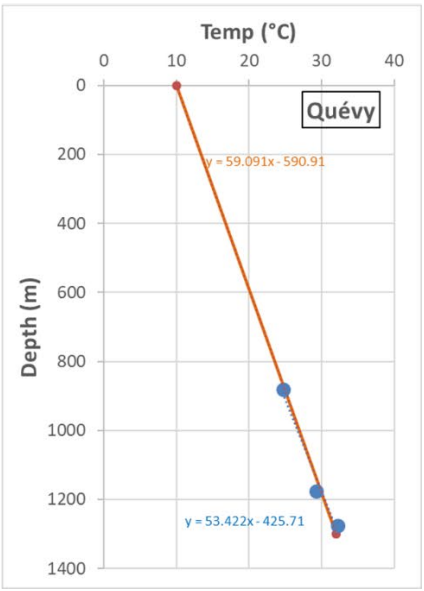
Temp (°C)
Quévy
y = 59.091x - 590.91
y = 53.422x - 425.71
Depth (m)

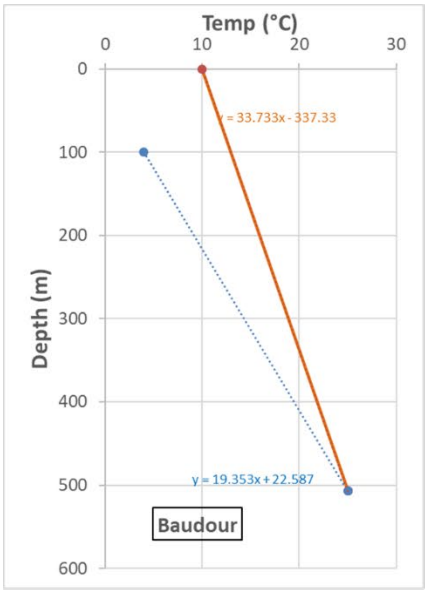
Temp (°C)
Depth (m)
y = 33.733x - 337.33
y = 19.353x + 22.587
Baudour

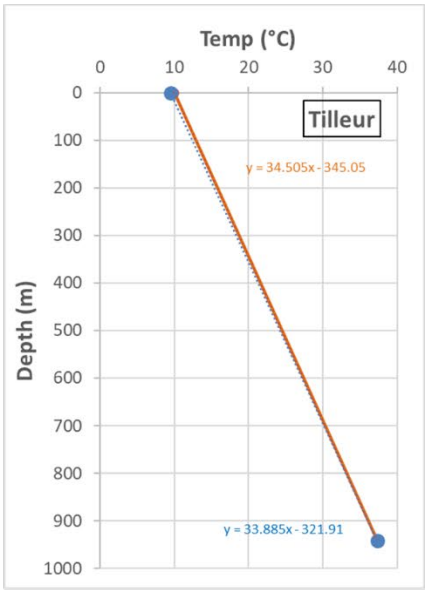
Temp (°C)
Depth (m)
Tilleur
y = 34.505x - 345.05
y = 33.885x - 321.91

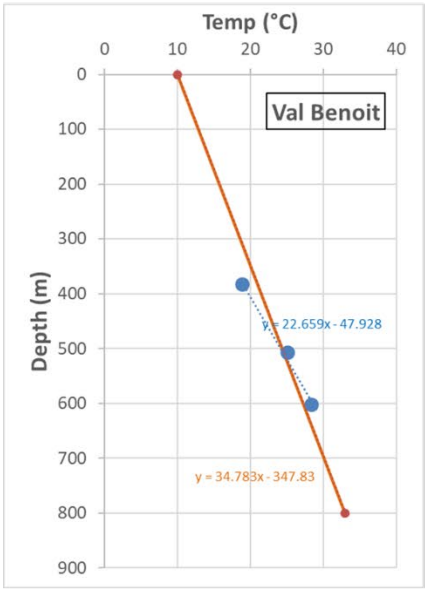
Temp (°C)
Depth (m)
Val Benoit
y = 22.659x - 47.928
y = 34.783x - 347.83

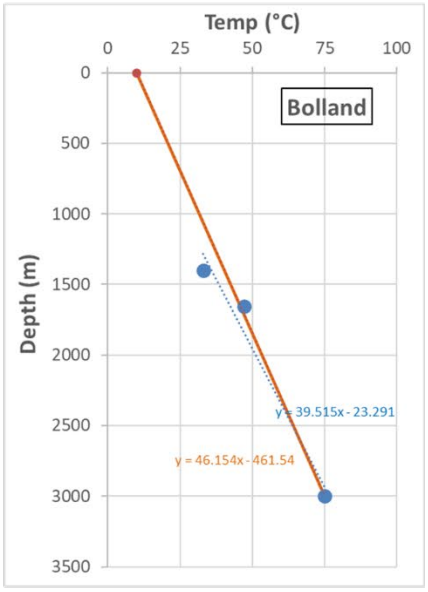
Temp (°C)
Depth (m)
Bolland
y = 39.515x - 23.291
y = 46.154x - 461.54

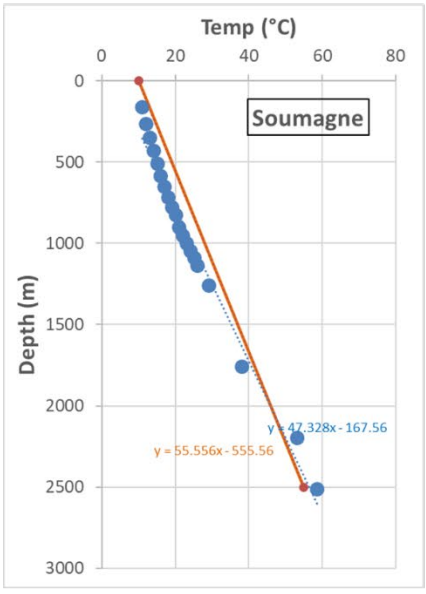
Temp (°C)
Depth (m)
Soumagne
y = 47.328x - 167.56
y = 55.556x - 555.56

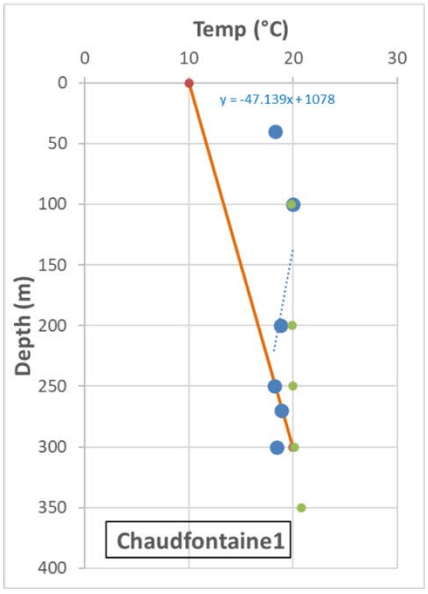
Temp (°C)
Depth (m)
y = -47.139x + 1078
Chaudfontaine1

PROJECT PARTNERS

Geologischer Dienst NRW

Fraunhofer IEG

vito

Geoscience for a sustainable Earth brgm

ebn

DMT

Geological Survey of Belgium

TECHNISCHE UNIVERSITÄT DARMSTADT

TNO innovation for life

RWE

PROJECT SUP-PARTNERS

RUHR UNIVERSITÄT BOCHUM RUB

GeoThermal ENGINEERING

MORE INFORMATION

Dr Martin Salamon (Project Manager)

Martin.Salamon@gd.nrw.de

+49 2151 897 230

www.nweurope.eu/DGE-Rollout

@DGE–ROLLOUT

SUPPORTED BY

europiZe UG

Dr Daniel Zerweck

+49 176 6251 5841

www.europize.eu

europiZe realising projects